UCLA
UCLA Previously Published Works

Title
Emission Line Properties of Seyfert Galaxies in the 12 μm Sample

Authors
Malkan, Matthew A
Jensen, Lisbeth D
Rodriguez, David R
et al.

Emission Line Properties of Seyfert Galaxies
In the 12 Micron Sample

Matthew A. Malkan[1], Lisbeth D. Jensen[1], David R. Rodriguez[1], Luigi Spinoglio[2], and Brian Rush[1,3]

malkan@astro.ucla.edu

ABSTRACT

We present optical and ultraviolet spectroscopic measurements of the emission lines of 81 Seyfert 1 and 104 Seyfert 2 galaxies which comprise nearly all of the IRAS 12μm AGN sample. We have analyzed the emission-line luminosity functions, reddening, and other diagnostics. For example, the narrow-line regions (NLR) of Seyfert 1 and 2 galaxies do not significantly differ from each other in most of these diagnostics. Combining the $H\alpha/H\beta$ ratio with a new reddening indicator–the [SII]6720/[OII]3727 ratio, we find the average $E(B-V)$ is 0.49 ± 0.35 for Seyfert 1's and 0.52 ± 0.26 for Seyfert 2's. The NLR of Sy 1 galaxies has only insignificantly higher ionization level than in the Sy 2's. For the broad-line region (BLR), we find that the C IV equivalent width correlates more strongly with [O III]/$H\beta$ than with UV luminosity. Our bright sample of local active galaxies includes 22 Seyfert nuclei with extremely weak broad wings in $H\alpha$, known as Seyfert 1.9's and 1.8's, depending on whether or not broad $H\beta$ wings are detected. Aside from these weak broad lines, our low-luminosity Seyferts are more similar to the Sy2's than to the Sy 1's. In a a BPT diagram we find that Sy 1.8's and Sy 1.9's overlap the region occupied by the Sy 2 galaxies. We compare our results on optical emission lines with those obtained by previous investigators using AGN subsamples from the Sloan Digital Sky Survey. The luminosity functions of forbidden emission lines [OII]$\lambda3727$Å, [OIII]$\lambda5007$Å, and [SII]$\lambda6720$Å in Seyfert 1's and 2's are indistinguishable. They all show strong downward curvature. Unlike the LF's of Seyfert galaxies measured by the Sloan Digital Sky Survey, ours are nearly flat at low luminosities. The larger number of faint Sloan "AGN" is attributable to their inclusion of weakly emitting LINERs

[1]Physics and Astronomy Department, University of California, Los Angeles, CA 90095

[2]Istituto di Fisica dello Spazio Interplanetario, INAF, Via Fosso del Cavaliere 100, I-00133 Roma, Italy

[3]Jet Propulsion Laboratory, California Institute of Technology, Pasadena, CA 91109

and H II+AGN "composite" nuclei, which do not meet our spectral classification criteria for Seyferts.

In an Appendix, we have investigated which emission line luminosities can provide the most reliable measures of the total non-stellar luminosity, estimated from our extensive multi-wavelength database. The hard X-ray or near-ultraviolet continuum luminosity can be crudely predicted from either the [O III]λ5007Å luminosity, or the combination of [O III]+Hβ, or [N II]+Hα lines, with a scatter of $\pm$ 4 times for the Sy 1's and $\pm$ 10 times for the Sy 2's. Although these uncertainties are large, the latter two hybrid (NLR+BLR) indicators have the advantage of predicting the same HX luminosity independent of Seyfert type.

Subject headings: galaxies: luminosity function — galaxies: Seyfert — quasars: emission lines

1. Introduction

Many previous studies have measured emission line ratios in samples of Seyfert nuclei, but the existence of strong selection effects (such as searches based on host galaxy properties, UV-excess or X-ray flux) raise questions about whether these results would hold for a representative sample of the *full* unbiased Seyfert population. A common limitation of most surveys is lack of complete data for the less luminous Seyfert nuclei. Another limitation of surveys at optical, ultra-violet, or soft X-ray wavelengths is their inability to find more reddened AGN. These limitations can be overcome with a nonstellar-flux-limited all-Sky survey at long wavelengths, which includes most of the bright Seyfert galaxies in the local universe. We pursue this approach in this paper. One of our motivations is that a better observational understanding of the nearest and best observed Seyfert galaxies will help us to understand the population of AGN at high redshifts. High-redshift studies are now seeking to measure the cosmic evolution of AGN, but with much less complete data than we have locally. By emphasizing quality of the data over raw quantity, we hope to use extensive observations of local AGN to help calibrate the emission-line diagnostics in high-redshift samples.

1.1. The Extended 12μm and CfA AGN Samples

The extended 12μm galaxy catalogue of Spinoglio & Malkan (1989) and Rush et al. (1993), is a 12μm flux-limited sample containing 893 galaxies selected from the IRAS Faint Source Catalog, Version 2. The galaxies in this catalogue have galactic latitude of $|b| \geq 25^o$

to decrease the extinction and avoid stellar contamination from the plane of our Galaxy. The 12μm galaxy sample contains 9 percent Sy 1's and quasars, and 11 percent Sy 2's. These percentages are of course far higher than the percentages of Seyferts among ordinary optically-selected galaxies such as in the Sloan Digital Sky Survey (SDSS). This is because, by design, the 12μm galaxies were selected at a wavelength where the continuum emission from warm dust in the Seyfert nucleus is especially bright relative to the normal emission from the underlying host galaxy. The 12μm flux is a constant fraction of $\sim 1/5$ of the bolometric flux in Seyfert 1 and 2 galaxies, three times more than in normal spiral galaxies (Spinoglio & Malkan 1989). The 12μm Seyferts are excellent representatives of the entire class, since they span nearly 6 orders of magnitude in luminosity. With a $\log(N) - \log(S)$ test Spinoglio & Malkan (1989) showed that the sample is complete down to 0.30 Jy, and has a level of incompleteness of $\sim 40\%$ at 0.22 Jy, the chosen flux limit.

The extended 12μm sample includes the brightest nearby Seyferts in the local universe. It has been subjected to extensive observational follow-up across the entire electromagnetic spectrum, and thus has the most complete multi-wavelength dataset available for any AGN sample. The redshifts range from $z = -0.0001$ to $z = +0.1884$, with the majority at $z \leq 0.05$. The redshifts are obtained from the the NASA/IPAC Extragalactic Database (NED)[1]. Throughout we adopt $H_0 = 72$ km/s/Mpc when computing distances to the Seyferts. [2].

To further control possible selection bias, we supplement the data with Seyfert galaxies from the Center for Astrophysics (*CfA*) galaxy sample. The *CfA* galaxies are a host-galaxy flux-limited, spectroscopically selected sample defined by Huchra et al. (1983). They come from 2399 galaxies with $m \leq 14.5$, with cuts in b and δ to avoid contaminations from the galactic plane (Huchra & Burg 1992). Thuan & Sauvage (1992) provide IRAS fluxes for 1544 galaxies in the *CfA* sample that are detected in the IRAS Faint Source Catalog. The overlap between the *CfA* and the 12μm sample is 47 Seyfert galaxies ($\sim 25\%$), as described in Rush et al. (1993).

Our data are compiled from multiple literature sources, the *CfA* sample, and our own previously unpublished data. The full sample, containing 185 Seyfert galaxies, 81 Seyfert 1's and 104 Seyfert 2 galaxies, is listed in Tables 1 and 2. It lists spectral classifications, redshift, and which galaxies are common to both the 12μm and *CfA* samples.

For simplicity we have adopted the spectral type classification given in NED's "Basic

---

[1] The NASA/IPAC Extragalactic Database (NED) is operated by the Jet Propulsion Laboratory, California Institute of Technology, under contract with the National Aeronautics and Space Administration.

[2] The one exception is NGC 3031/M81, for which we use the measured Cepheid distance of 3.63 Mpc (Freedman et al. 1994).

Data". These are based on spectra obtained from a wide variety of publications. The ability to discern faint Balmer-line wings–required for an Sy 1 classification–depends on the quality the spectrum. The classification for weak Sy 1's and also composite Sy 1+HII galaxies is therefore sometimes ambiguous. But we only have one or two active galaxies for which our data indicate a different classification from NED. These special cases are mentioned below.

1.2. Spectroscopic Measurements

We have averaged over multiple measurements and conservatively assign an uncertainty of 30% in the line fluxes, although ratios of nearby lines are usually more accurate. Our combined optical and ultraviolet emission lines and their corresponding rest wavelengths can be found in Table 3. Optical line fluxes along with literature references are in Table 4, and the UV data are summarized in Table 5, also with literature references.

We have supplemented our observational results with data from Sloan Digital Sky Survey Data Release 7 from "The MPA-JHU DR7 release of spectrum measurements"[3]. This data base contain 927,552 AGN galaxies. We excludeed two-thirds of those which lacked S/N emission-line ratios of at least > 10. We have also used the SDSS DR6 SkyServer Explore Tool[4] to provide line fluxes for 5 Sy1's and 11 Sy 2's, including four objects (IRAS 13354+3924, IRAS 16146+3549, NGC 833, and UGC 6100) for which no prior data existed. We calculate the line-flux ratios of [O III]/Hβ, [O III]/[O II], [O II]/[O I], [N II]/Hα, [O II]/[S II], [O II]/[N II], [O III]/[S II], and [N II]/[S II], and find that the average difference between our sample and that of SDSS for the ratios is -0.03 ± 0.25, consistent with no systematic difference.

This paper is organized as follows. In § 2 we describe our emission line luminosity functions. In § 3 we use emission lines to diagnose properties in the narrow line region, while in § 4 we consider the broad line region. We summarize our results in § 5. In Appendix A we investigate, which, if any, emission line luminosities can provide the most reliable estimates of the total non-stellar luminosity,

---

[3]Obtained   from   http://wwwmpa.mpa-garching.mpg.de/SDSS/DR7/.   Raw   data   from http://wwwmpa.mpa-garching.mpg.de/SDSS/DR7/raw_data.html.

[4]The SDSS DR6 SkyServer Explore Tool can be found at `http://cas.sdss.org/astro/en/tools/explore/`.

2. Line Luminosity Functions

We construct emission-line luminosity functions (LFs) for each Sy 1 and Sy 2 galaxy by taking V_{max} values from the 12μm flux sample and binning them according to their individual emission-line luminosities. Since our sample is defined and limited by the 12μm flux, we apply correction factors where necessary to account for incompleteness previously determined by Rush et al. (1993).

Emission-line LFs are derived for [O I], [O II], [O III], [N II], [S II], Hα, and Hβ lines. A double power-law in Logarithmic space is fitted to the luminosity functions:

$$\Phi(L) = \frac{\Phi_\star}{\left(\frac{L}{L_\star}\right)^\alpha + \left(\frac{L}{L_\star}\right)^{\alpha+\beta}} \tag{1}$$

where $L_\star$ is the emission-line luminosities of the characteristic break in the LF (in erg/s), and $\Phi_\star$ is twice the number density at that break (in Mpc^{-3}). The points always require a bend in the LF, i.e. a steeper slope at high luminosities. However, the strength of this bend is not well determined due to the small of high- and low-luminosity galaxies in our sample. We therefore assumed a low-luminosity slope of $\alpha = -0.1$ and a slope steepening break of $\beta = +1.5$. These broken power laws, based on the shape of the 12μm LF, match all the emission line LFs adequately.

The best-fit parameters of the LFs are given in Table 6 and displayed in Figure 1. We plot the LF for the narrow lines [O II] and [O III], and the Hα and Hβ lines (with the broad and narrow components combined) in Figure 1.

The Balmer-line luminosity function of the Sy 1s extends to higher luminosities than that of the Sy 2s. Because the Sy 1 permitted lines are brightened by the contribution from their broad line region (BLR), they are more numerous at the high line luminosities. However, for the [O III] and [O II] LFs, there is only a small difference between the Sy 1 and Sy 2 galaxies. Thus at a given narrow line luminosity, the two types of Seyferts have similar space densities. There is also little difference in the 12μm Sy 1 and Sy 2 continuum LFs (Rush et al. 1993; Toba et al. 2014), at luminosities below that of quasars. So if the narrow line luminosity is emitted approximately isotropically, the similarity of these Sy1 and Sy2 space densities suggests that the 12μm continuum emission is also relatively isotropic.

Figure 1a, 1c, and 1d compares the Sy 1 and Sy 2 emission-line Luminosity Functions for our 12μm selected sample with the optically selected AGN sample from the SDSS (Hao et al. 2005; Simpson 2005). The optical and IR selection methods show good agreement in the derived LFs around the 'knee', i.e. the line-luminosities around 10^{39-41} erg/s, for both Seyfert types. However, compared with the 12μm selection, the SDSS finds relatively *more* low-

luminosity AGN and relatively *less* high-luminosity AGN. Thus the SDSS LFs are steeper at low luminosities than our 12μm sample. The SDSS LFs thus show much weaker breaks to high luminosities. We attribute this difference to the inclusion in SDSS of more "composite" Sy 2's. These low-luminosity AGN have substantial line emission contributed by star formation, which tends to prevent them for being classified in NED as Seyfert Galaxies. On the other hand, the 12μm selection is particularly efficient for finding luminous AGN, which tend to be at high redshifts. Figure 1 indicates that it is the optical selection of SDSS that becomes significantly incomplete at high luminosities (emission-lines $\gtrsim 10^{41}$). We note that the [O III] LF found by Bongiorno et al. (2010) from zCOSMOS, at slightly higher redshifts ($0.15 < z < 0.3$) agrees closely with ours, and is similarly flatter than that of Hao et al. (2005).

We have also compared our Seyfert galaxy LF's to the those of the local normal galaxies in Hα and [O III] (not shown), using data from Gallego et al. (1995, 1996). For most line luminosities, the space density of the galaxies without Seyfert nuclei exceeds that of the Seyfert by up to two orders of magnitude. However, the Hα and [O III] LF's of non-AGN cut off exponentially above $L_{line} > 10^{41}$ erg/sec. The result is that with Hα or [O III] luminosities of 10^{41} erg/sec or above, most of the galaxies are Seyferts.

3. Seyfert 1 and 2 Narrow Line comparison

The main observational difference between the two types of Seyfert galaxies is the presence or absence of broad permitted lines with widths of 10^3 km/s or higher. The Seyfert 1 galaxies are further divided into Seyfert 1.2, 1.5, 1.8, and 1.9's, based on the increasing relative strength of the Narrow to Broad line components (Osterbrock 1981).

In this Section we investigate differences and similarities in the emission line properties of Seyfert 1 and 2 galaxies in our sample. Although we consider a galaxy with *any* broad lines to be a Sy 1, we keep in mind the possibility that Seyferts with only very weak wings on Hβ (Sy 1.8), or only on Hα (Sy 1.9), may turn out to be more similar to Seyfert 2 galaxies in most observational respects.

3.1. Nuclear Reddening

Various physical models have been proposed to connect Sy 1 and Sy 2 galaxies. The "unification model" assumes that the sole difference is the viewing orientation of the Seyfert nucleus with respect to our line of sight (Antonucci 1993). Thus there would be no dif-

ference between the Sy 1 and the Sy 2 nuclei if these galaxies were viewed from the same direction. There are, however, alternate hypotheses. For example, in the Galactic Dust Model (Malkan et al. 1998), Sy 2's have intrinsically larger dust covering fractions due to the presence of galactic dust lanes. This dust obstructs our view of the inner nuclear regions where the engine and broad line region (BLR) are located. One consequence is that the emission lines in Sy 2's should on average have a greater degree of reddening than Sy 1's.

To test this we compare two optical emission line-ratios in our data that are widely separated in wavelength–the Balmer decrement (Hα/Hβ) and the narrow line region (NLR) ratio [O II]/[S II]. The positive correlation between these two reddening-sensitive line ratios is shown in Figure 2. We note that both the Sy1's and the Sy2's appear to lie along the same correlation. Furthermore, this trend looks similar to the one defined by emission-line galaxies measured in the SDSS, which are shown by the cloud of small grey/green points. There are 135,116 galaxies of any origin (AGN or starburst) with spectra from DR7, which have all four emission lines detected at greater than the 10-sigma level.

To quantify this trend, we compute proper least-squares fits for these groups of galaxies separately. For this and all subsequent correlation analyses, we used a proper least-squares (LSQ) fit (to account for the comparable errors in both line ratios). We use a `FORTRAN` fitting program (*Linear regression with measurement errors and scatter*[5]) written and described by Akritas & Bershady (1996), to compute the orthogonal proper LSQ fits. The slope of the fit for the 12μm sample is 0.44 ± 0.14 for the Sy 1 Galaxies and 0.44 ± 0.22 for the Sy 2's. The large sample of SDSS emission line galaxies also shows a similar line-ratio correlation, with a slope of 0.33 ± 0.004 and intercept of 0.64 ± 0.08. For comparison we calculate the predicted slope in this line ratio correlation that should be produced solely by reddening of two fixed (constant) intrinsic line ratios. Adopting the standard reddening law of Cardelli et al. (1989) for $R = 3.1$, the predicted reddening slope should be 0.44. We placed the straight-line reddening vector in the upper left in Figure 2 with tick marks showing increasing amounts of $E(B - V)$.

The quantitative fits confirm the visual impression of the figure: all three of the groups of galaxies (Sy1s, Sy2s, and SDSS emission line galaxies) show a consistent correlation. The positive slopes of each correlation are all consistent with each other, and with the prediction from a standard reddening law. The Seyfert galaxies have more widely ranging line ratios than those normally seen in the SDSS spiral galaxies, although the distributions mostly overlap. We also compared the $H\alpha/H\beta$ and [S II]/[O II] ratios with two other emission-line ratios that should be sensitive to reddening. However, these other line ratios–[N II]/[O II]

---

[5]Obtained from the website for statistical packages: http://www2.astro.psu.edu/statcodes/sc_correlregr.html.

and [O III]/[Ne III]–did not correlate so well the others, suggesting that they are influenced by other factors beyond mere reddening. Thus, their intrinsic value can not be considered constant, and we do not consider them valid reddening indicators. The results of all the correlations are presented in Table 8.

There is reasonable consistency with the position of the lower-left (bluest) extent of the line ratios in all three galaxy groups. This limit should correspond to galaxies with essentially unreddened emission-line regions. We therefore interpret this lower left boundary as indicating that both types of Seyferts, as well as normal star-forming galaxies, have roughly the same intrinsic (unreddened) line ratios. Specifically, the line ratios in both Sy1s and Sy2s have unreddened $H\alpha/H\beta$ ratios which appear consistent with *Case B'* ($\log H\alpha/H\beta$ = 0.5), (Gaskell & Ferland 1984), also recommended by Malkan (1983)). The normal spiral galaxies from SDSS have slightly lower Balmer decrements–they are consistent with the normal Case B value of $\log H\alpha/H\beta = 0.45$, although this small difference is only marginally significant.

Supported by the consistency of the $(H\alpha/H\beta)$ correlation with [S II]/[O II], we will now assume that the primary determinant of where each galaxy lies in Figure 2 is its amount of internal dust reddening. We therefore estimated $E(B-V)$ values in each Seyfert galaxy assuming the standard reddening law and intrinsic line ratios found above. The average of the two line ratio estimators gives the $E(B-V)$ values for individual Seyfert galaxies plotted in Figure 3. This histogram shows that the average reddening is the same in both Seyfert types: $< E(B-V) >= 0.49 \pm 0.35$ for the Sy1's, and $< E(B-V) >= 0.52 \pm 0.26$ for the Sy2's. A Kolmogorov-Smirnov (K-S) test yields a probability of $p(0.31)$ that the two groups are drawn from the same distribution. In both Seyfert classes, $E(B-V)$ ranges uniformly from 0.0 to 1.0 mag. Furthermore, there is no trend for reddening to vary systematically with the luminosity of the Seyfert galaxy, over more than two orders of magnitude in 12 μm luminosity. For comparison, the average $E(B-V)$ inferred from normal SDSS spirals is 0.63 mag. As shown in Figure 2, the Seyfert reddenings strongly overlap with these, except for the larger scatter which may be due to observational uncertainties.

Other studies have been done on reddening in Seyfert galaxies. Rhee & Larkin (2005) report substantial reddening in the narrow-line regions of 11 Seyfert 2 galaxies[6] and Tsvetanov & Iankulova (1989) also finds that Sy 2's are more reddened than the Sy 1's for their sample of 24 Seyferts. However, Malkan (1983) found only a marginal tendency for Seyfert 1's to have smaller reddening in their forbidden line region, consistent with our new findings. Our finding of no significant difference between the reddening of the NLRs in Seyfert 1 and Seyfert 2 galaxies

---

[6]These include Seyfert 1.8 and 1.9 galaxies.

is consistent with the expectation of the strong unification hypothesis.

We note that some narrow line regions appear to be optically thick at optical wavelengths, with $E(B-V) > 0.8$ mag, which implies $A_V > 2.5$. If this reddening is also applied to the non-stellar continuum, then the UV would be more then 99% extinguished – i.e. virtually obliterated. It appears that some minority of the Seyfert nuclei we uncover in the 12 μm sample–unlike many other samples–are so reddened that some special explanation is required for their observed UV continuum emission. The two possibilities are:

1. The UV continuum is purely from the stellar photospheres in the host galaxy. If the UV continuum is particularly bright, this would be coming from a young population of hot stars.

2. The observed UV continuum does come from the non-stellar engine (thought to be an accretion flow around the central massive black hole), but suffers from less extinction than the NLR. For example, we might have indirect unobscured views to the central engine, which we see through scattered light (Antonucci 1993).

In most cases neither of these possibilities can be ruled out.

3.2. Degree of Gas Ionization

The blue portion of the optical spectrum contains several emission line ratios which are sensitive to the level of ionization in the gas. Table 3 summarizes the ionization potential of our emission lines. We select line ratios that differ in their ionization potential by 20 eV or more. These diagnostic line ratios are observable by CCD spectrographs up to redshifts of $z \sim 0.9$.

As summarized in Table 7, our averages for $\log([\text{Ne V}]/[\text{Ne III}])$ are -0.07 ± 0.24 and -0.16 ± 0.40 (individual scatter) for 32 Sy 1's and 26 Sy 2's, respectively. For $\log([\text{O III}]/[\text{O II}])$ the averages are 0.59 ± 0.51 and 0.43 ± 0.52 for 50 Sy 1's and 51 Sy 2's, respectively. For both line ratios, the K-S test shows that the small differences between the Sy1's and Sy 2's are not significant at the 95% level [7].

---

[7] This finding contradicts Schmitt (1998). A possible explanation is the Schmitt (1998)'s selection of 52 Sy 1 galaxies from the literature may have missed some low-luminosity Sy 1's. They are included in our complete sample, and tend to have less highly ionized narrow lines. The only possible significant ionization difference seen in our sample is that $\log([\text{Ne III}]/[\text{O III}])$ is -0.17 ± 0.40 in the Sy 1's and -0.48 ± 0.30

In Figure 4 we plot log[O III]/Hβ versus log[Ne III]/[O II]. The dotted line is a model for the NLR from Groves et al. (2004). The numbers along the line indicate the ionization parameter $U = S_\star/(nc)$, where $S_\star$ is the flux of ionizing photons and n is the number density of hydrogen atoms. Their model is of a dusty, radiation pressure-dominated region surrounding a photo-evaporating molecular cloud, which in turn is surrounded by a coronal halo where the dust has been largely destroyed (Dopita et al. 2002). In this model only the NLR is included. The particular model that matches our data is un-reddened and un-depleted. Groves et al. (2004) adopt a power-law ionizing continuum, $F_\nu \propto \nu^\alpha$ with the best slope of $\alpha = -1.4$, and a number density of 10^3 cm^{-3}. The chemical abundances are solar. As can be seen in Figure 4, the Sy 1's are generally in the lower/right of the dotted line in the graph, while the Sy 2's are to the left and above. Since Hβ is a broad line and the BLR is not included in this particular model, we expect the Sy 1's to have lower log[O III]/Hβ values. The NLR ratios indicates an ionization parameter of $\log U = -2.5$ for the average of the Sy 1's, and -2.8 for the average of the Sy 2's.

3.3.   [S II]/[N II] Ratio

We found that the log([S II]/[N II]) line ratio has almost the same value for Sy 1's and Sy 2's, -0.23 ± 0.24 and -0.28 ± 0.20 respectively, with a K-S probability of $p(0.97)$. For the previously selected subset of Seyfert 2 galaxies we took from DR7, we find an average value of $\log([SII]/NII])$ of -0.19 ± 0.1. This is also reasonably consistent with our values, allowing for observational uncertainties (Figure 6). An average value of -0.23 ± 0.18 for this ratio can be used regardless of whether the galaxy is a type 1 or type 2 Seyfert. These lines have about the same ionization potential (10.4 and 14.5 eV), but their critical densities are different ($\sim 10^3$ cm^{-3} for [S II] and $\sim 10^5$ cm^{-3} for [N II]). The fact that this ratio is the same for both Seyfert types implies that the density structure of the narrow line region is the same at least up to 10^5 cm^{-3}. This is consistent with the result found by Nagao, Murayama, & Taniguchi (2001). They find that the ratio [S II]/[N II], among other low-ionization line ratios, shows no difference between Sy 1's and Sy 2's. Our [S II]/[N II] ratio is the same as that found in Sy 1 galaxies in (Stern & Laor 2013). They obtained log([S II]/[N II]) = -0.25, independent of bolometric luminosity, for the mean stellar mass in their sample $< \log M_* \sim 10.8 >$. We caution that, in the least-massive galaxies with

---

in the Sy 2's. However, many of the measurements of "[Ne III]" in the Sy 1's were obtained with low-resolution spectroscopy, with moderate SNRs. We therefore suspect that some of the line flux attributed to [Ne III]λ3869 in some Sy 1's in our study, and in Schmitt's, may instead be contaminated from the weak broad line emission line He Iλ3889.

$< \log M_* \sim 10.4 >$, (Stern & Laor 2013) found slightly higher ratios of $\log([S\ II]/[N\ II])$ $\gtrsim -0.20$. Since we do not generally know M_* for all Seyfert host galaxies, this introduces a small uncertainty that might contribute to the scatter we observe. Nonetheless, the near constancy of the [S II]/[N II] can be useful in de-blending [N II] from broad Hα in Sy 1's. Some studies use other forbidden line fluxes to remove the [N II] which is blended with Hα (Lacy et al. 1982).

3.4. Warm Dust

Our IRAS data give the ratio $f_{25\mu m}/f_{60\mu m}$ integrated over each entire galaxy, which increases when the proportion of warm dust (heated by the AGN) increases. The [O III]/[O II] ratio was previously used as a measure of the the relative strength of the Seyfert nucleus with respect to the H II regions in the host galaxy. We plot [O III]/[O II] vs. $f_{25\mu m}/f_{60\mu m}$ (Figure 5), and find a positive correlation for both Seyfert types. A Kendall's Tau test reveals that this gas ionization/dust temperature correlation holds for both Sy 1's and Sy 2's separately, with confidence levels of CL = 99.9% and CL = 97.5% respectively. The individual regression fits for the Sy galaxies are $\log([O\ III]/[O\ II]) = (0.97 \pm 0.12)\log(f_{25\mu m}/f_{60\mu m})$ + (1.03 ± 0.63) for the Sy 1 and $\log([O\ III]/[O\ II]) = (0.69 \pm 0.16)\log(f_{25\mu m}/f_{60\mu m})$ + (0.85 ± 0.76) for the Sy 2 types.

3.5. Correlation of [OI] and [OIII]

The ionization potential of O I is 13.6 eV and the critical density of [O I]λ6300Å is 1.8×10^6 cm^{-3} (De Robertis & Osterbrock 1986). The [O I] line is formed beyond the classical ionization front, in a partially ionized region heated by X-rays from the AGN (Veilleux & Osterbrock 1987; Spinoglio & Malkan 1992; Groves et al. 2004). We therefore test the possibility that [O I] correlates better with the high-ionization fine structure emission lines of the Seyfert NLR, than with the low-ionization emission lines from H II regions. In Figure 7 we plot the narrow line ratios $\log$[O II]/[O III] vs. $\log$[O I]/[S II]. As we found in other NLR plots, the vertical axis is inversely proportional to the average ionization level of the gas, and therefore increases in the relatively "weak" Seyferts, which have larger contributions to their [O II] line emission from H II regions in their host galaxies. If the main difference along the horizontal axis is also degree of gas ionization, then we would expect a positive correlation in this graph. Instead, we find the opposite–an *inverse* correlation. The orthogonal regression fit for the Sy 2 galaxies is: $\log([O\ II]/[O\ III]) = (-1.2 \pm 0.12)$ $\log([O\ I]/[S\ II]) - (1.11 \pm 1.72)$. Although the spread is large, we find that a strong cor-

relation exists (Kendall's Tau > 99%). The Sy 1 sample also gives a fit with a negative slope: $\log([\text{O II}]/[\text{O III}]) = (-0.36 \pm 0.16)\log([\text{O I}]/[\text{S II}])$ - (0.71 ± 1.17). Here the Kendall's Tau is < 90% and the null hypotheses can not be rejected, i.e. the Sy 1 correlation is not significant. But for Seyferts, overall, the [O I] line tracks [O III] more closely than the [O II] line.

Since this conclusion comes from the small dataset of our 12μm Seyferts, we sought confirmation of this same inverse correlation in the much larger database of the SDSS DR7. From this database of > 900,000 galaxies, we restricted our consideration to 239,795 galaxies in which the [NII], Hα, and [OIII] emission lines were detected at the 10-σ level or better, while the [OII] line was detected at the 20-σ level. Using TOPCAT[8] to plot these line ratios in the standard BPT diagram, we used the Select Tool feature to construct a subset of 15,190 "pure" Seyfert galaxies, whose emission spectra are dominated by the NLR. These DR7 Seyferts are plotted in the figure with small grey/green dots, which were fitted by the solid gray/green line with the proper LSQ. This fit is indistinguishable from what we obtained fitting our much smaller Sy2 sample, but with a larger scatter ($\log([\text{O II}]/[\text{O III}]) = (-1.3 \pm 0.87)\log([\text{O I}]/[\text{S II}])$ - (1.10 ± 0.42)). Thus SDSS confirms the trend we found that [O I]$\lambda6300$Å tracks the high-ionization gas in Seyferts more closely than the low-ionization gas, because both are produced primarily by the AGN, not HII regions. [9]

3.6. BPT Diagram

The BPT diagrams (Baldwin, Phillips, & Terlevich 1981) were developed to identify different photoionization mechanisms in galaxies, using ratios of lines at similar wavelengths, to minimize the effects of reddening. In general, galaxies dominated by stellar photoionization in H II regions have relatively stronger emission lines from less ionized gas, like [O II] and [N II]. Active galaxies, in contrast, have a power-law ionizing continuum, which tends to produce more lines from highly ionized gas. In addition, X-rays from the AGN can penetrate into neutral or partially ionized zones to produce low-ionization lines that would typically not be produced in H II regions. Thus AGN emission line spectra show a wider *range* of ionization.

The most common BPT diagram uses the ratio of [O III]/Hβ to [N II]/Hα, though sometimes [S II] or [O I] is used in place of [N II]. These diagrams are designed for narrow-line

---

[8]Available at http://www.star.bris.ac.uk/~mbt/topcat/.

[9]This finding holds for Seyfert nuclei, *not for LINERs* (see also Netzer (2009)).

objects, and therefore the Sy 1 galaxies are generally not displayed because of the presence of broad permitted lines. However, we decided to include the weak broad-line objects to determine where they would be located in the BPT diagram, for situations in which the BLR and NLR are not separated.

Our BPT diagram is shown in Figure 8. The gray/green dots represent all 239,795 SDSS DR7 galaxies with highly significant detection in all four emission-lines. We include the heavy dashed-dot line from Kauffmann et al. (2003) defined by: $\log([OIII]/H\beta) > 0.61/[\log([NII]/H\alpha)-0.05]+1.3$, which separates H II regions from active galaxies. The light dotted line from Kewley et al. (2001) defined by: $\log([OIII]/H\beta) > 0.61/[\log([NII]/H\alpha)-0.47)]+1.19$, also excludes "composite" galaxies which include too much emission form H II regions to be classified as "pure" AGN.

The Sy 2 Galaxies cluster in the upper right of the BPT diagram, around $(x,y) = (0.05, 0.85)$. However, a significant minority of the Sy 2 galaxies fall close to the Kauffman boundary: 17 out of a total of 82 Sy 2's (21%), would be classified as "composite" (Seyfet 2 + HII) galaxies. This contamination of narrow emission line fluxes from the host spiral galaxy is especially serious for less luminous AGN, when they are observed with relatively poor spatial resolution (Theios et al. 2016).

3.7. BPT Classification of Broad Line AGN

The BLR contamination should in principle be removed before using the narrow line for BPT classification. However, in some studies the spectra do not or cannot have the broad Balmer components removed. This is especially true if the BLR component is very faint compared to the NLR. We therefore plot the total line-flux ratios (broad + narrow components) for Sy 1.5, 1.8, 1.8 and Sy 2 galaxies in Figure 8. In addition to the AGN/HII boundary line from Kauffmann et al. (2003) we also plot the boundary line defined by Kewley et al. (2001). The Sy 1.9 galaxies occupy the same region as the Sy 2's (except for NGC 7314 which has a very weak nucleus and is located below the AGN/HII boundary line). This is because their broad Balmer line components are so weak. Thus the BLR hardly alters the ratio of forbidden lines to the permitted lines, away from the NLR values. This agrees with the findings of Simpson (2005), who showed that his "Sy 1.x galaxies" having broad $H\alpha$ wings (what we call Sy 1.8 and Sy 1.9's) are indistinguishable from the Sy 2's in the BPT diagram. Indeed, Simpson's NLR mixing line - also plotted in Figure 8 - goes through most of our Sy 1.8's and Sy 1.9's, with the latter lying further away from the AGN/HII boundary. Our few Sy 1.8's are all at an intermediate location in the BPT diagram. Their combination of NLR and BLR compontents make them appear like *composite AGN* - mixtures of HII and

Seyfert 2 line emissions. The distribution of our own 12 μm Seyferts in the BPT diagram is somewhat similar to that of the hard X-ray selected Seyferts from the BAT survey (Oh 2017). However, our sample includes more low-luminosity Sy 2's. Their line emission is more dominated by HII regions. The relatively weaker NLR emission corresponds to lower hard X-ray luminosity (see Appendix A). Thus they are likely to be missed by the BAT survey. Another difference is that a substantial fraction of the BAT Seyfert 1's fall left of the NLR area in the BPT diagram. Their [N II]/Hα ratios are anomalously low. This could have resulted from mistakenly attributing some of their broad Hα emission to the NLR component.[10]

(Stern & Laor 2013) used SDSS spectra of 3175 Sy 1 galaxies to separate out the narrow line components of Hα and Hβ. This allowed them to place the pure NLR line ratios on the BPT diagram. Since we did not make this BLR/NLR decomposition, we can only compare the their results to our own Sy 2's and Sy 1.9's, since they have negligible contribution from the broad Balmer lines. (Stern & Laor 2013) found that the BPT ratios classify 5% of the NLRs in their Sy 1 sample as "Star-Forming galaxies" (i.e. below the Kauffman line) and 15% of them as HII/AGN (i.e. "Composites", between the Kauffman and Kewley lines). Our narrow-line Seyferts show exactly the same distribution: three out of 65 are classified as Star-Forming, while 12 out of 65 are classified as Composites. Thus the BPT distribution of our NLR AGN sample is indistinguishable from SDSS Seyfert 1's.

3.7.1. Quantative Decomposition of AGN Components in the BPT Diagram

To quantitatively interpret the location of AGNs in this BPT diagram, we make the simplifying assumption that each galaxy has observed emission lines which are the sums of three "pure" Seyfert 1, 2, and LINER components. To accomplish this crude separation we have adopted the values for log([N II]/Hα) of -1.1, 0.05, 0.2 and log([O III]/Hβ) of -0.1, 0.85, 0.1, for the three respective components. The solid lines in Figure 8 connect each of these three components, showing the ' mixing curves" obtained by combining varying proportions of two of our "pure" components. Along the perimeter we have omitted the third emission component; for the interior points we compute the contribution from all three types.

To determine the relative contribution from each particular type, we take the distance,

---

[10]The BPT diagram is supposed to include only the narrow emission lines. When their broad emission lines are not removed, their contamination would push Sy galaxies to the left downward as in Figure 8. Indeed, the BLR-dominated Seyferts nearly all fall below the AGN/HII separation line. For all the 32 Seyfert galaxies classified as any type of broad line AGN (1, 1.2, 1.5, 1.8 and/or 1.9) we find that according to the definition of the BPT diagram 59% and 75% of them lie below the Kauffman and Kewley lines, respectively.

d_i in the BPT diagram of each Seyfert to the three points defined as pure Seyfert 1, 2, and LINER. The contribution is defined as

$$C_i = \frac{1/d_i}{\displaystyle\sum_i 1/d_i} \tag{2}$$

where i refers to Seyfert 1, 2, and LINER emission components, and

$$d_i^2 \;=\; \left(\log \frac{[OIII]}{H\beta} - \left(\log \frac{[OIII]}{H\beta}\right)_i\right)^2$$

$$+ \left(\log \frac{[NII]}{H\alpha} - \left(\log \frac{[NII]}{H\alpha}\right)_i\right)^2. \tag{3}$$

Our three-component decompositions of the relative AGN contribution are shown graphically in Figure 8. The resulting components for individual galaxies are shown in Figure 9.

The average BPT contributions of the "BLR" and "NLR" components change from 72%/6% in pure Sy 1's to 56%/17% in Sy 1.5's, to 43%/12% in Sy 1.8's, and to 20%/58% in Sy 1.9's. In this highly simplified BPT decomposition, all types of Seyfert 1 nuclei show an average contribution of 24% from a "LINER" component, regardless of the BLR/NLR ratios.

As Figure 8 indicates, actual AGN show a continuously ranging mixture of NLR and LINER components. There is no clear-cut separation between the two components. However, an emission line galaxy cannot be reliably classified as predominantly a LINER unless it shows a $> 50\%$ contribution from the LINER component. The dot-dashed "mixing curve" in Figure 8 shows the locus along which the LINER component, C_{LINER}, equals 50%. As we expected, the only galaxies lying to of the right of the boundary are classified as LINERs (the rightmost filled circle is NGC 2639, classified in NED basic data as a Sy 1.9, but based on its Activity Type it is considered a LINER). Interestingly, this line corresponds to the transition between LINERs and Seyfert galaxies in Groves et al. (2004). That is, our $C_{LINERs} = 50\%$ line accurately divides most of the Groves et al. (2004) Seyferts from the LINERs–the blue and the red datapoints, respectively in their Figure 1. As expected from our use of NED classification, hardly any of our Seyfert galaxies turn out to be LINER-dominated. The same result applies to the BAT-selected survey (Oh 2017).

4. Broad Line Region, Eigenvector 1, and the Baldwin Effect Relationship

The luminosities of broad emission lines generally increase linearly with the non-stellar continuum luminosity, but there are some exceptions. Baldwin (1977) found a negative

correlation between the equivalent width of C IVλ1549Å, and UV continuum luminosity ($L_{UV} = \nu L_\nu$ λ1449Å) in quasars, commonly referred to as the *Baldwin effect*. This less-than-linear increase in C IV with underlying luminosity has been confirmed in many different quasar and Sy 1 samples (Jensen et al. 2016). One interpretation is that the wavelength peak of accretion disk luminosity shifts from the UV in quasars to the EUV in the less luminous Seyferts, because the latter have smaller black holes with hotter accretion disks (Zheng & Malkan 1993).

Our sample includes 23 Sy 1 galaxies with measured C IV emission lines (Table 5). We exclude the galaxies MKN 231 and NGC 2841 galaxies because of their anomalously weak C IV. Figure 10a shows a plot of log(C IV EW) versus log($L_{UV}/10^{40}$) (color coding is described in the following section). The solid line shows our proper least-squares fit to this Baldwin relation

$$\log(CIVEW) = (-0.12 \pm 0.05) \log\left(\frac{L_{UV}}{10^{40}}\right) + (2.4 \pm 0.16). \tag{4}$$

The amplitude of this slope is much smaller than what Baldwin (1977) found for his sample of 20 quasars (-0.63). These is so much scatter in our sample that the anti-correlation is only weakly significant.

4.1. Improving the Baldwin Effect with Eigenvector 1

Many studies have attempted to connect the Baldwin effect with some other parameter, which could be more astrophysically fundamental than L_{UV} (Zheng & Malkan 1993). The most significant way in which the emission-line regions of quasars differ from each other is in the strength of the so called 'Eigenvector 1' (Boroson & Green 1992). This parameter is associated with stronger [O III] from the NLR, which is in turn strongly anti-correlated with the permitted Fe II emission lines from the BLR. Boroson & Green (1992) also reported that EW of [O III] and the luminosity of [O III] are both correlated with Eigenvector 1. They suggested that a weaker Eigenvector 1 results when the Eddington ratio (L/L_{Edd}) is larger. Our sample does not contain reliable Fe II measurements. We therefore use the [O III]/Hβ ratio instead to indicate the strength of Eigenvector 1.

We coded the Seyfert galaxy points in Figure 10a by their [O III]/Hβ ratio. Those with log([O III]/Hβ) > 0.28 are shown as red squares; Seyferts with weaker [O III]/Hβ are shown as blue diamonds. The strong segregation between the red and blue points shows that the [O III]/Hβ is indeed a good a predictor of EW(C IV). To find out how good, we plot log(C IV

EW) versus $\log([\text{O III}]/\text{H}\beta)$ in Figure 10b. It shows a significant positive correlation:

$$\log(CIVEW) = (0.42 \pm 0.1) \log \left(\frac{[OIII]}{H\beta} \right) + (2.11 \pm 0.27). \tag{5}$$

with a $\chi^2/dof = 1.11$ for 22 degrees of freedom. This new "substitute Baldwin relation" works much better than the original ($\chi^2/dof = 1.48$, 21 degrees of freedom). We can also see this in Figure 10b by the color coding. Seyferts with $\log(\text{L}_{UV}) > 43.15$ as blue diamonds, while the less luminous galaxies are shown as red squares. The large overlap of red and blue points in this graph demonstrates that L_{UV} is not so good predictor of EW(C IV) as is $[\text{O III}]/\text{H}\beta$. Our finding of a positive correlation between EW (CIV) and Eigenvector 1 in Seyfert 1 nuclei is fully consistent with Baskin and Laor's finding of a similar correlation in the PG Quasars (Baskin & Laor 2004).

Could both L_{UV} and $[\text{O III}]/\text{H}\beta$ be combined to make an even better Baldwin relation? We made a bivariate least-squares fit:

$$\log(CIVEW) = (2.16 \pm 0.1) + (-0.02 \pm 0.04) \log \left(\frac{L_{UV}}{10^{40}} \right) + (0.37 \pm 0.12) \log \left(\frac{[OIII]}{H\beta} \right) \tag{6}$$

The coefficient of the UV luminosity is only slightly negative, not significantly different from zero. In contrast, the coefficient of $\log([\text{O III}]/\text{H}\beta)$ differs from zero by 3σ, indicating that the Baldwin effect may be tightened by either adding this optical line ratio or replacing L_{UV} altogether. We use the Bayesian Information Criterion difference (ΔBIC) to compare the bivariate fit in Eqn. 6. The parameters from the original Baldwin effect (Eqn. 4) give a $BIC = 96.93$ and the new "substitute Baldwin relation" gives $BIC = 89.11$. The inclusion of the $[\text{O III}]/\text{H}\beta$ in the Baldwin relation give $\chi^2/dof = 1.15$ and $BIC = 85.79$. The ΔBIC between L_{UV} and the bivariate fit is > 10. Thus the original Baldwin relation, using L_{UV} is significantly inferior. The ΔBIC obtained when adding L_{UV} to the regression (Eqn. 6) is 3.32, which is considered only marginal evidence in favour of adding L_{UV}. Evidently, Eigenvector 1 may be a more fundamental driver of the Baldwin effect. Perhaps L_{UV} is only a secondary parameter–it might correlate inversely with EW(CIV) merely because it correlates inversely with $\log([\text{O III}]/\text{H}\beta)$. We graph this relation in Figure 10c, and indeed there is a strong anticorrelation: $\log(\text{L}_{UV}) = (-2.57 \pm 0.66)\log([\text{O III}]/\text{H}\beta) + (2.57 \pm 1.51)$ (Kendall's Tau $> 99\%$ significance).

Our data also show a weak positive correlation between EW(C III]1909) and $[\text{O III}]/\text{H}\beta$. However, there is so much scatter that, unlike with the EW(C IV), this does not provide a meaningful Baldwin relation. We also plot $\log(\text{Mg II}/[\text{O II}])$ versus $\log([\text{O III}]/\text{H}\beta)$ in Figure 11. The solid black line shows the fit to the broad-line objects only (Sy 1's are

indicated by red traingles). The best fit slope is very significantly non-zero (-0.93 ± 0.12), i.e. the anti-correlation is significant at the 99% level. Since we use [O III]/Hβ as our proxy for "Eigenvector 1", this anti-correlation shows that the relative strength of Mg II decreases in strong "Eigenvector 1" Seyfert 1 galaxies. Although we lack sufficient Fe II data for our 12μm sample, this suggests the UV Mg II and optical Fe II emission line strengths should be closely correlated. The average log(Mg II/[O II]) ratio in the NLR alone (Seyfert 2's) is -0.99 ± 0.63.

5. Conclusions

We have shown that the narrow-line regions of Seyfert 1's and Seyfert 2's galaxies have little systematic difference in many properties:

1. The luminosity functions of the narrow lines are the same for both types of Seyferts. Therefore the space densities of Seyfert 1 and Seyfert 2 galaxies are roughly equal. (Only the Hα and Hβ luminosity functions differ in Sy 1's at higher luminosities.)

2. Measured by two independent emission-line ratios (Hα/Hβ and [S II]/[O II]), the Sy 2's are not more reddened than the Sy 1's. This indicates that the amount of dust present in the narrow line region in both types of Seyferts is similar. Nor do the Sy1's show a significantly higher ionization in their NLRs, also consistent with the premise of simple geometric unification. We have demonstrated that a value of -0.25 ± 0.16 can be used for log([S II]/[N II]), regardless of whether the galaxy is a type 1 or 2 Seyfert. This can be useful in determining the flux of [N II] when it is blended in Hα.

3. We identify several ratios indicative of the ratio of the AGN luminosity to that of the host galaxy (the "Seyfert dominance"). For example the dust in Seyfert galaxies is warmer for those objects more dominated by their AGN contribution than by their starburst or H II region contributions. And we have found that [O I]λ6300Å correlates most closely with the high-ionization lines, both being powered primarily by the AGN. In the BPT diagram, we find that 15 % of our Seyfert galaxies would be classified by Kauffmann et al. (2003) as "HII/AGN Composites". A further 5 % have such a weak Seyfert nuclei that their spectra are not distinguishable from those of normal star-forming spiral galaxies.

4. By separating the Seyfert galaxies into sub-types ($1+1.2+1.5$ and $1.8+1.9$) we showed that Seyfert 1.8 and 1.9 galaxies have similar ionization levels to Sy 2's. The Sy 1.8 and Sy 1.9's have very weak broad lines, so their narrow line ratios are similar to that

of Sy 2's. The BPT diagram demonstrates that these objects lie in the same area as Sy 2's as well.

5. We use the BPT diagram to make a simple decomposition of emission line ratios into three "pure" components –Sy1, Sy2, and LINERs. As expected, the relative importance of the Sy 1 component falls steadily from the Sy 1.2's to the Sy 1.5's, the Sy 1.8's, and finally the Sy 1.9's. Although AGNs show a continuous range in NLR/LINER ratios, we find that the LINER component needs to be $> 50\%$ for an AGN to be specroscopically classified as a LINER.

6. In the broad-line region we studied the Baldwin effect and found that C IV equivalent width correlates more strongly with [O III]/Hβ, rather than with UV luminosity. This may imply the Baldwin effect is more strongly dependent on the Eddington ratio, L/L_{Edd}. An additional implication was that broad Mg II emission correlates with Fe II.

A.   APPENDIX A. Emission Line Proxies for the Nonstellar Luminosity

Many previous studies pursued the goal of estimating the total non-stellar power of an AGN by simply measuring one of the strongest emission lines in its spectrum. Any such "shortcut", if reliable over a wide range of Seyfert galaxies, would be of value in analyzing large samples, where good data at all wavelengths may not be available. However, the danger of correlating any two luminosities against each other in astronomical samples is well known. When a wide range of luminosities is present, as in our Seyfert sample, an apparent correlation of one luminosity with another luminosity is often found, even when there may be little physical connection between the two quantities. Correlations of line luminosities with continuum luminosities in the 12μm Seyfert sample should be expected, and do not necessarily prove how they are linked.

Keeping this caveat in mind, we now examine these line/continuum correlations to determine the intrinsic scatter, possible non-linearities and systematic differences depending on which quantities and which AGN types are included. Our dataset–a representative sampling of a very wide range of local AGN properties–has advantages for finding and testing various "scaling relations" between emission lines and the broadband AGN continuum. The various AGN-powered luminosities we are seeking to correlate span almost six orders of magnitude in our Seyfert galaxies. Our estimates of non-stellar luminosities from the X-ray and UV to the IR are given in Table 10. It is important to base correlations on a complete sample, where the observed fluxes for nearly all the AGN are detections–not upper limits.

The key to all proposed scaling relations is finding easily measured quantities which are dominated by the non-stellar (AGN) component. We start with the most obvious non-stellar continuum – hard X-rays – since they are thought to be produced almost entirely by the central engine of the AGN, except at the lowest luminosities. As Brightman & Nandra (2011a) and others point out, it is very difficult for any galaxy lacking a Seyfert nucleus to produce (through normal stellar processes, including X-ray binaries) more than 10^{40} erg/sec in hard X-rays. In Figures 12a to 15a (top left in these panels) we compare the luminosities of several of the strongest optical emission lines with the hard X-ray luminosities (L_{HX}) reported by Brightman & Nandra (2011a,b); Panessa et al. (2008).

In the Sy 1's, L_{HX} is reasonably well correlated with $L_{H\alpha}$. The plotted lines assumed a linear correlation, i.e., fixing the slope in log(line) versus log(continuum) to be 1. There are no cases when a deviation from this linear slope gives a statistically superior fit. The result that $L_{HX} \sim 15L_{H\alpha}$ is not surprising, since it has long been known that the broad Balmer emission line luminosities are closely correlated with the non-stellar continuum (Yee 1980; Malkan & Sargent 1982). As summarized in Table 9, we find an individual scatter of a factor of 3 (solid blue squares in Figure 13a). This is far from perfect, but might be useful in cases where only a rough individual estimate, or average of a sample, is wanted.

A limitation of that relation is that a high-quality spectrum of the Hα region may not be available, so it is sometimes unclear whether an AGN should be classified as Sy 1 or Sy 2. Then this correlation runs into trouble, since Sy 2's lack any directly detectable broad Hα emission. They produce more hard X-rays for a given (narrow) Hα luminosity, and the scatter is so large it nearly destroys the HX/Hα correlation in Sy 2's.

To include both Sy 1's and Sy 2's in one single AGN correlation, we have followed previous studies, such as Tommasin et al. (2010). We considered whether the strongest emission from the NLR – the [O III]λ5007Å line – could instead serve as a proxy to measure the non-stellar luminosity (Mulchaey et al. 1994; Dasyra et al. 2008; Goto et al. 2011). Indeed, the blue symbols in Figures 14a and 15a do show that the [O III] luminosity can *roughly*

predict the HX luminosity, with an uncertainty of 4 times for Sy 1's and 10 times for Sy 2's. For a given $\lambda 5007$ line luminosity, the Sy 1's tend to be 30% brighter in hard X-rays. That is a small difference compared with the large intrinsic scatter.

Our $L_{\rm HX}/L_{\rm [OIII]}$ correlation for the Sy 1's has nearly the same normalization and scatter as Heckman (2005) found for local AGN selected by O III$\lambda 5007$Å ($L_{\rm HX}/L_{\rm [OIII]} = 10^{1.64}$ compared with our $L_{\rm HX}/L_{\rm [OIII]} = 10^{1.59}$). This is also the same correlation found by Xu et al. (1999) ($L_{\rm HX}/L_{\rm [OIII]} = 10^{1.60}$), as well as (Stern & Laor 2012), (their Equation 6). We find that the Sy 2's have relatively weaker hard X-rays and larger scatter in the $L_{\rm [OIII]}$ correlation. But this Sy 1/2 difference is larger in the Hao et al. (2005) sample, which includes a substantial tail of Sy 2's with very weak hard X-rays ($log(L_{\rm [OIII]}) = 39 - 41$). Hao et al. (2005) points out that the X-ray selected AGN will have relatively larger $L_{\rm HX}/L_{\rm [OIII]}$ ratios than our sample selected at longer wavelengths. Indeed this trend is seen in the luminous AGN sample found in Chandra Deep Field South Survey at $0.3 < z < 0.8$. The best fit correlation for AGN, found by Netzer (2006) is shown by the dashed line in Figures 14a and 15a. In contrast, up to $L_{\rm HX} \sim 10^{44}$ we see no evidence of non-linearities in the correlation with any of the emission-line fluxes.

But we can improve on using $L_{\rm OIII}$ as a general measure of AGN power. We are motivated by the Stern and Laor studies (papers II and III) of 3175 SDSS spectra of Sy 1 galaxies. (Stern & Laor 2012) showed that the luminosity of the broad component of Hα increase more rapid then the luminosities of any of the narrow lines. We propose to account for this simply by adding measures of NLR and BLR luminosities together. To include Seyferts of Type 1 and Type 2, we favor a "hybrid" indicator of non-stellar luminosity, the sum of the [O III] and Hβ lines - shown by the open symbols in Figures 14a and 15a. This empirical compromise captures the AGN luminosity in Sy 2's emerging in the NLR, but also the BLR luminosity in Sy 1's. And as shown by Table 10, one single relation, $L_{HX} \sim 25 L_{([OIII]+H\beta)}$, gives a rough estimate for any Seyfert galaxy, regardless of type.

The usefulness of this hybrid (NLR+BLR) AGN luminosity indicator lead us to also consider correlations with the blend of Hα+[N II] (open symbols in Figures 13a and 14a), which can be difficult to disentangle at low spectral resolution. The correlation with HX shows an extreme amount of scatter for the Sy 2's, but is still consistent with the same (tighter) correlation we find for Sy 1's. We therefore consider the combined Hα+[N II] line luminosity a possible "backup" predictor of non-stellar hard X-rays, which is also independent of Seyfert type: $L_{HX} \sim 11 L_{([NII]+H\alpha)}$. Since the broad H$\alpha$ and Hβ in Seyfert 1 galaxies vary with time, the non-simultaneity of our spectroscopy with the X-ray observations introduces some artificial scatter into these diagrams. However, the amplitude of variability is usually small enough that this increase in scatter is small compared to what is observed in

Runco, J., et al. (2016).

A.0.1. Less Reliable Continuum Proxies for the total Nonstellar Luminosity

The hard X-rays only carry a minority ($\leq 10\%$) of the bolometric luminosity of most AGN, and this fraction tends to be significantly lower in more luminous objects. We therefore also searched for emission line proxies which could predict non-stellar luminosity at longer wavelengths closer to the bolometric peak output of typical AGN. The near-UV luminosity of Sy 1's (around the peak of the "Big Blue Bump" (Malkan & Sargent 1982)), tends to be about four to five times the HX. As we found for the hard X-rays, the NUV luminosities can also be predicted by our combined [O III] and [O III]+Hβ luminosities, with similar scatter (± 4 times for the Sy 1's, and ± 9 for the Sy 2's), shown in Figures 12b to 15b. Our normalization of $L_{UV} \sim 200 L_{[OIII]}$ and $L_{UV} \sim 100 L_{([OIII]+H\beta)}$ for Sy 1s are similar to the range of models in Netzer (2006), assuming bolometric luminosity is a few times L_{UV}.

However, these emission line correlations with NUV luminosity have very different normalizations: for a given line luminosity, the Sy 2's produce 3 to 8 times *more* NUV than the Sy 1's. Although we are correlating observed luminosities, this discrepancy is not explained by extinction differences, since we did not find strong Sy 1/Sy 2 differences in optical estimates of $E(B - V)$, and the non-stellar UV continuum extinction should be even larger. Instead, a plausible explanation is that the UV continuum in Sy 2's is dominated by recently formed hot stars which were also included in the large GALEX beam, outshining a possible AGN contribution.

Next, we made an even less reliable effort to isolate the non-stellar nuclear continuum, using the 1.2 μm, 1.6 μm, and 2.2 μm luminosities of the central pixels in 2MASS images of each Seyfert nucleus (Figures 12c to 15c). We decomposed the near-IR luminosities of the nucleus into contributions from the AGN and starlight, both assumed to have constant colors. The uncertainties in deriving the 2.2 μm luminosities of the weaker AGN are at least a factor of 2 by this so-called "color given" method (Malkan & Filippenko 1983). The correlations of line luminosities with this non-stellar 2 μm luminosity are even weaker than with the HX and NUV, with very large scatter for both Sy 1's and Sy 2's. The only line luminosity predictor worth possibly considering is the sum of [O III]+Hβ , which when multiplied by 15 gives a rough prediction for the non-stellar 2.2 μm luminosity of any Seyfert nucleus, regardless of type. And our same backup line ratio, the sum of Hα+[N II], when multiplied by by 5.5, gives a rough prediction, with the Sy 2 nuclei being on average 40% brighter at 2.2 μm .

Our final estimator of the non-stellar AGN luminosity was made from small-beam photometry at 10 μm, from Gorjian et al. (2004) (Figures 12d to 15d). The correlations with the line luminosities are too poor to be of much use, with worse than a factor of ten scatter. The 10 μm correlation with [O III] luminosity is the same for Sy 1's and Sy 2's, perhaps because both are thought to originate in the NLR.

Five of the broad-line AGN in our sample are LINERs which have been found to exhibit weak broad-line components, usually faint extended wings under Hα (Ho et al. 1997b). We have included these with the Seyfert 1's in Figure 13, but plotted with stars and 'x' symbols, not boxes. We were surprised to see that these AGN, which Ho et al. denotes as "LINER 1's" also follow roughly the same correlations between emission lines and non-stellar continuum as do the normal Sy 1's.

Similarly, a dozen of the narrow-line AGN in our multi-wavelength sample are now best classified as LINERs, and we included them in the panels of Figures 13 and 15, along with the normal Sy 2's, except plotted with star symbols. Within the large scatter of the non-stellar line/continuum luminosity correlations, we again note that the LINERs lacking any broad wings overlap entirely with the Sy 2s. Our results would hardly have changed whether they were included or excluded in the linear fits. Given the large scatter in these emission-line/continuum luminosity correlations, they cannot be used to separate various AGN types, even LINERs.

REFERENCES

Akritas M. G. & Bershad M. A.1996 ApJ, 470, 706

Antonucci, R., 1993, ARA&A, 31, 473

Armus, L., Heckman, T. M., & Miley, G. K. 1989, ApJ, 347, 727

Baldwin, J. A. 1977, ApJ, 214, 679

Baldwin, J. A., Phillips, M. M., Terlevich, R., 1981, PASP, 93, 5

Barr, P., Willis, A. J., & Wilson, R. 1983, MNRAS, 203, 201

Baskin, A. & Laor, A. 2004, MNRAS, 350, 31

Bonatto, C. J., & Pastoriza, M. G. 1997, ApJ, 486, 132

Bongiorno, A., Mignoli, M., Zamorani, G., Lamareille, F., et al. 2010, A&A, 510, A56

Boroson, T. A. & Green, R. F. 1992, ApJS, 80, 109

Boroson, T. A., & Meyers, K. A. 1992, ApJ, 397, 442

Brightman, M. & Nandra, K, MNRAS, 413, 1206

Brightman, M. & Nandra, K, MNRAS, 414, 3084

Buson, L. M. & Ulrich, M.-H. 1990, A&A, 240, 247

Cardelli, J. A., Clayton, G. C., Mathis, J. S. 1989, ApJ, 345, 245

Clavel, J., Benvenuti, P., Cassatella, A., Heck, A., Penston, M. V., Selvelli, P. L., Beeckmans, F., & Macchetto, F. 1980, MNRAS, 192, 769

Clavel, J., & Joly, M. 1984, A&A, 131, 87

Colbert, E. J. M., Baum, S. A., Gallimore, J. F., O'Dea, C. P., Lehnert, M. D., Tsvetanov, Z. I., Mulchaey, J. S., & Caganoff, S. 1996, ApJS, 105, 75

Coziol, R., Pena, M., Demers, S., & Torres-Peimbert, S. 1993, MNRAS, 261, 170

Cruz-Gonzalez, I., Carrasco, L., Serrano, A., Guichard, J., Dultzin-Hacyan, D., & Bisiacchi, G. F. 1994, ApJS, 94, 47

Dasyra, K. M., Ho, L. C., Armus, L., Ogle, P.; Helou, G., Peterson, B. M., Lutz, D., Netzer, H., Sturm, E. 2008, ApJ, 674L, 9

de Grijp, M. H. K., Keel, W. C., Miley, G. K., Goudfrooij, P., & Lub, J. 1992, A&A, 96, 389

De Robertis, M. M. & Osterbrock, D. E., 1986, ApJ, 301, 727

De Robertis, M. M., Hutchings, J. B., & Pitts, R. E. 1988, AJ, 95, 1371

Dopita, M. A., Groves, B. A., Sutherland, R. S., Binette, L., & Cecil, G. 2002, ApJ, 572, 753

Farrah, D., Surace, J. A., Veilleux, S., Sanders, D. B., & Vacca, W. D. 2005, ApJ, 626, 70

Ferland, G. J., & Osterbrock, D. E. 1986, ApJ, 300, 658

Freedman, W. L., Hughes, S. M., Madore, B. F., et al. 1994, ApJ, 427, 628

Gallego, J., Zamorano, J., Aragon-Salamanca, A., & Rego, M. 1995, ApJ, 455, L1

Gallego, J., Zamorano, J., Rego, M., Alonso, O., & Vitores, A. G. 1996, A&AS, 120, 323

Gaskell, C. M. & Ferland, G. J., 1984, PASP, 96, 393

Gorjian, V., Werner, M. W., Jarrett, T. H., Cole, D. M., Ressler, M. E. 2004, ApJ, 605, 156

Goto, T., Arnouts, S., Malkan, M., , et al., 2011, MNRAS, 414, 1903

Grandi, S. A. 1983, ApJ, 268, 591

Groves, B. A., Dopita, M.A., Sutherland, R.S. 2004, ApJS, 153, 9

Groves, B. A., Heckman, M.H., Kauffman, G. 2006, MNRAS, 371, 1559

Hao, L., Strauss, M. A., Fan, X., , et al., 2005, AJ, 129, 1795

Heckman, T. M, Ptak, A., Hornschemeier, A., Kauffmann, G. 2005, ApJ, 634, 161

Ho, L. C., Filippenko, A. V., & Sargent, W. L. W. 1996, ApJ, 462, 183

Ho, L. C., Filippenko, A. V., & Sargent, W. L. W. 1997, ApJS, 112, 315

Ho, L. C., Filippenko, A. V., Sargent, W. L. W., & Peng, C. Y. 1997, ApJS, 112, 391

Ho, L. C., & Peng, C. Y. 2001, ApJ, 555, 650

Huchra, J., Davis, M., Latham, D., Tonry, J. 1983, ApJS, 52, 89

Huchra, J. & Burg, R., 1992, ApJ, 393, 90

Jensen, T.W., Vivek, M., Dawson, K.S., Anderson, S.F., Bautista, J., et al. 2003, ApJ, 833, 199

Kauffmann, G., Heckman, T. M., Tremonti, C., et al., 2003, MNRAS, 346, 1055

Kewley, I., Dopita, M.A., Sutherland, R. S., Heiser, C. A., & Trevena, J. 2001, ApJ, 556, 121

Kim, D.-C., Sanders, D. B., Veilleux, S., Mazzarella, J. M., & Soifer, B. T. 1995, ApJS, 98, 129

Kirhakos, S. D., & Steiner, J. E. 1990, AJ, 99, 1722

Kishimoto, M., Antonucci, R., Cimatti, A., Hurt, T., Dey, A., van Breugel, W., & Spinrad, H. 2001, ApJ, 547, 667

Kraemer, S. B., Wu, C.-C., Crenshaw, D. M., & Harrington, J. P. 1994, ApJ, 435, 171

Kuraszkiewicz, J. K., Green, P. J., Forster, K., Aldcroft, T. L., Evans, I. N., & Koratkar, A. 2002, ApJS, 143, 257

Kuraszkiewicz, J. K., Green, P. J., Crenshaw, D. M., Dunn, J., Forster, K., Vestergaard, M., & Aldcroft, T. L. 2004, ApJS, 150, 165

Lacy, J. H., Malkan, M., Becklin, E. E., Soifer, B. T., Neugebauer, G., Matthews, K., Wu, C.-C., Boggess, A., & Gull, T. R., 1982, ApJ, 256, 75

Lumsden, S. L., Heisler, C. A., Bailey, J. A., Hough, J. H., & Young, S. 2001, MNRAS, 327, 459

Malkan, M. A. & Sargent, W. L. ApJ, 254, 22

Malkan, M. A., 1983, ApJ, 264, L1

Malkan, M. A. & Fillipenko, A.V. 1983, ApJ, 268, 562

Malkan, M. A., & Oke, J. B. 1983, ApJ, 265, 92

Malkan, M. A., Gorjian, V., & Tam, R. 1998, ApJS, 117, 25

McQuade, K., Calzetti, D., & Kinney, A. L. 1995, ApJS, 97, 331

Misselt, K. A., Clayton, G. C., & Gordon, K. D. 1999, PASP, 111, 1398

Moran, E. C., Halpern, J. P., & Helfand, D. J. 1996, ApJS, 106, 341

Morris, S. L., & Ward, M. J. 1989, ApJ, 340, 713

Morton, D. C., 2003, ApJS, 149, 205

Mulchaey, J. S., Koratkar, A., Ward, M. J., Wilson, A. S., Whittle, M., Antonucci, R. R. J., Kinney, A. L., & Hurt, T. 1994, ApJ, 436, 586

Nagao, T., Murayama, T., & Taniguchi, Y. 2001, PASJ, 53, 629

Netzer, H., 2006, A&A, 453, 525

Netzer, H., 2009, MNRAS, 399, 1907

Oh, K., 2017, MNRAS, 464, 1466

Osterbrock, D. E. 1981, ApJ, 249, 462

Osterbrock, D. E., & Martel, A. 1993, ApJ, 414, 552

Osterbrock, D. E. & Ferland, G. J., 2006, Astrophysics of Gaseous Nebulae and Active Galactic Nuclei, Second Edition (Sausalito, California: University Science Books)

Panessa, F., Bassani, L., de Rosa, A., et al. 2008, A&A, 483, 151

Poggianti, B. M., & Wu, H. 2000, ApJ, 529, 157

Polletta, M., Bassani, L., Malaguti, G., Palumbo, G. G. C., & Caroli, E. 1996, ApJS, 106, 399

Reynolds, C. S., Ward, M. J., Fabian, A. C., & Celotti, A. 1997, MNRAS, 291, 403

Rhee, J. H. & Larkin, J. E., 2005, ApJ, 620, 151

Rodríguez-Ardila, A., Pastoriza, M. G., & Donzelli, C. J. 2000, ApJS, 126, 63

Runco, J., Cosens, M., Bennert, V. N., et al. 2016, ApJ, 821, 33

Rush, B., Malkan, M. A., Spinoglio, L. 1993, ApJS, 89, 1

Schmitt, H. R. 1998, ApJ, 506, 647

Simpson C., 2005, MNRAS, 360, 565

Sosa-Brito, R. M., Tacconi-Garman, L. E., Lehnert, M. D., & Gallimore, J. F. 2001, ApJS, 136, 61

Spinoglio, L. & Malkan, M. A., 1989, ApJ, 342, 83

Spinoglio, L. & Malkan, M. A., 1992, ApJ, 399, 504

Stearn, J.& Laor, A., 2013, MNRAS, 426, 2703

Stearn, J.& Laor, A., 2013, MNRAS, 431, 836

Storchi-Bergmann, T., Kinney, A. L., & Challis, P. 1995, ApJS, 98, 103

Theos, R., Malkan, M. & Ross, N. 2016, ApJ, 822, 45

Thuan, T. X. 1984, ApJ, 281, 126

Thuan, T. X. & Sauvage, M. 1992, A&AS, 92, 749

Toba, Y., Oyabu, S., Matsuhara, H., Malkan, M. A., et al. 2014, ApJ, 788, 45

Tommasin, S., Spinoglio, L., Malkan, M. A., Fazio, G. 2010, ApJ, 709, 1257

Tsvetanov, Z. I. & Iankulova, I. M., 1989, MNRAS, 237, 707

Veilleux, S. & Osterbrock, D. E., 1987, ApJS, 63, 295

Veilleux, S., Kim, D.-C., Sanders, D. B., Mazzarella, J. M., & Soifer, B. T. 1995, ApJS, 98, 171

Veilleux, S., Kim, D.-C., & Sanders, D. B. 1999, ApJ, 522, 113

Wang, T.-G., Zhou, Y.-Y., & Gao, A.-S. 1996, ApJ, 457, 111

Wang, T.-G., Lu, Y.-J., & Zhou, Y.-Y. 1998, ApJ, 493, 1

Winkler, H. 1992, MNRAS, 257, 677

Xu, C., Livio, M., Baum, S., et al. ApJ, 118, 1169

Yee, H. K. (1980), ApJ, 241, 894

Young, S., Hough, J. H., Efstathiou, A., Wills, B. J., Bailey, J. A., Ward, M. J., & Axon, D. J. 1996, MNRAS, 281, 1206

Zheng, W. & Malkan, M. A., 1993, ApJ, 415, 517
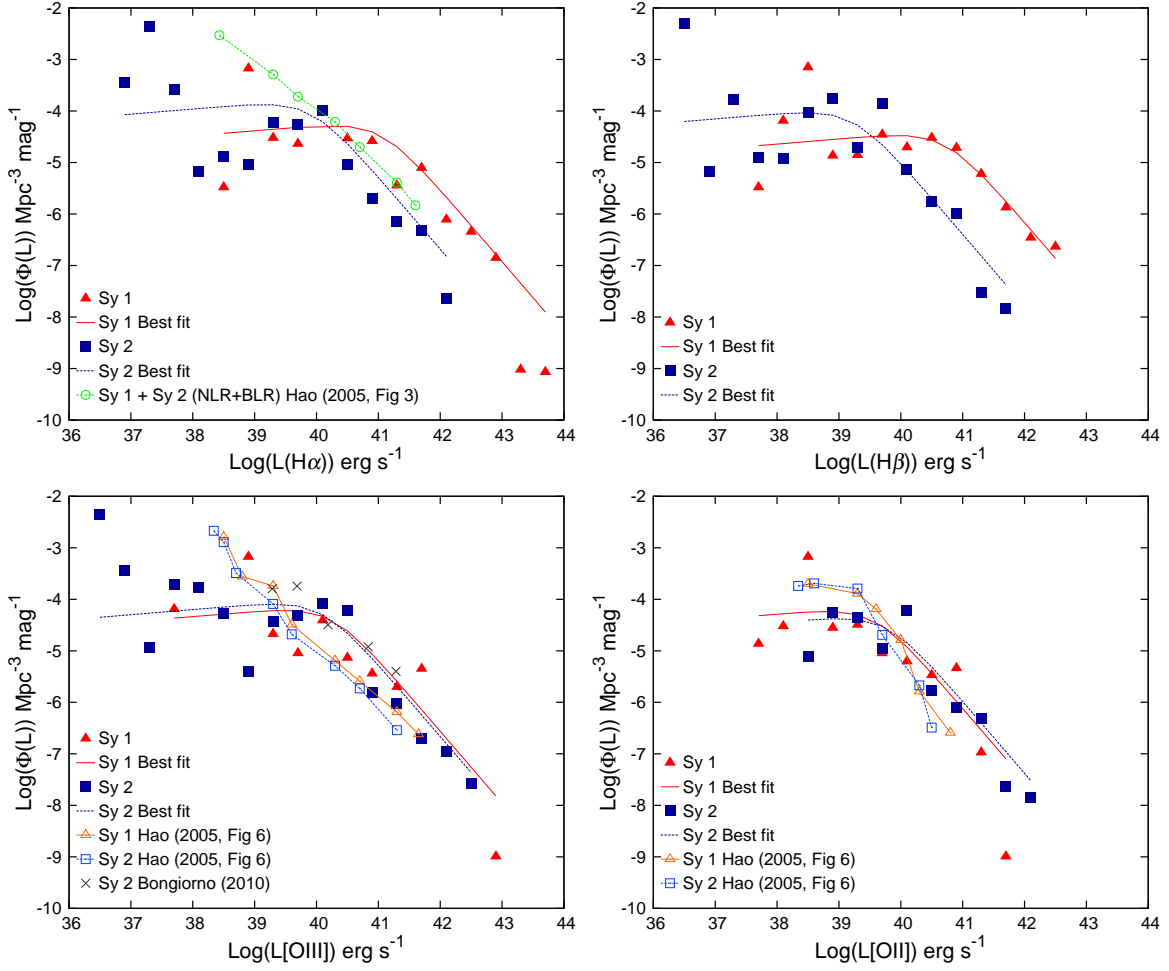
Fig. 1.— Emission Line Luminosity Functions for Hα, Hβ, [O III] λ5007, and [O II], where Φ has units of Mpc^{-3} mag^{-1} and L has units of ergs s^{-1}. The solid line is the fit to the Seyfert 1 LF's, while the blue line is the fit to the Seyfert 2's. In the graphs of LF for Hα, [O III], and [O II] we have overplotted the Luminosity Functions of SDSS Seyfert galaxies from Hao et al. (2005). In the panel for [O III] we have also added LF data from Bongiorno et al. (2010) (zCOSMOS). Although data from Hao et al. (2005) covers our z range ($0 < z < 0.15$), the zCOSMOS data ($0.15 < z < 0.35$) agrees better with our LF's.
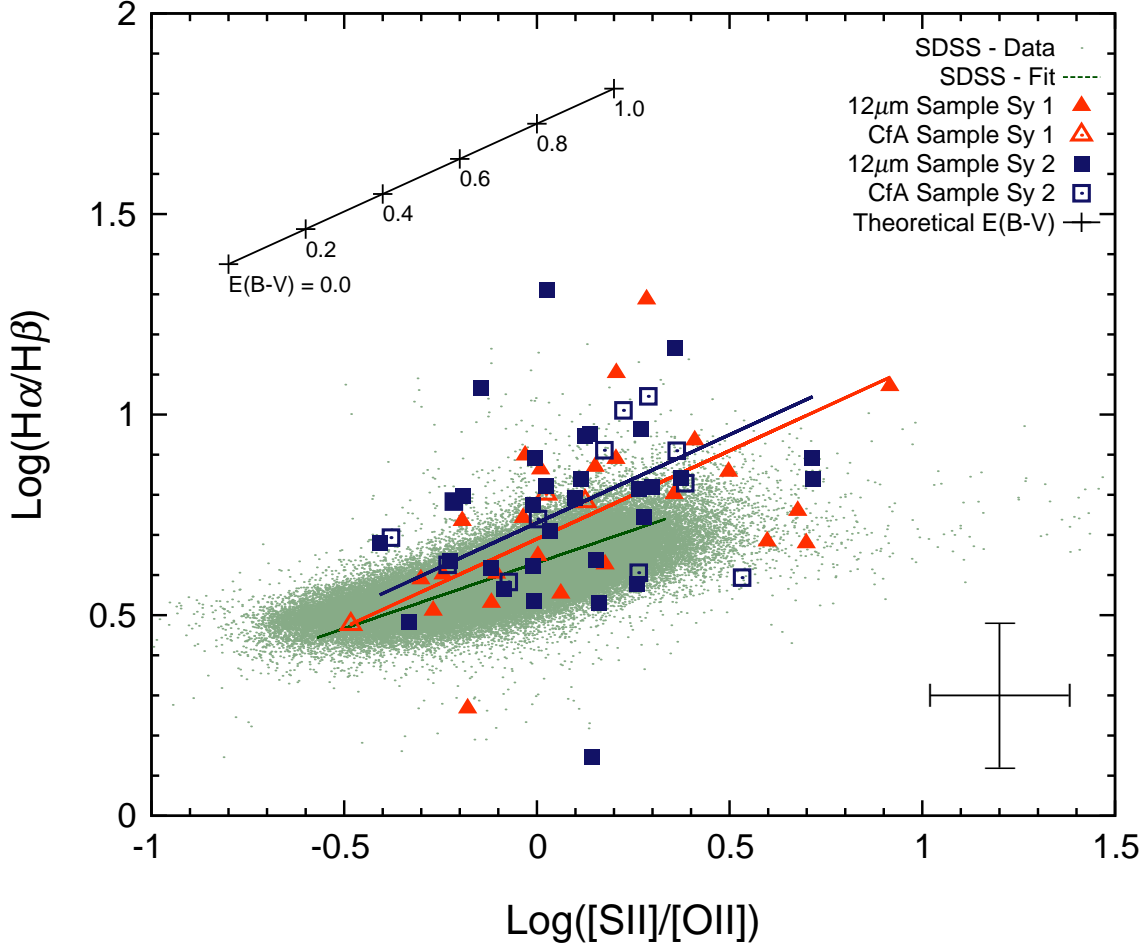
Fig. 2.— Nuclear reddening-sensitive emission-line ratios $\log(\mathrm{H}\alpha/\mathrm{H}\beta)$ vs. $\log([\mathrm{S\ II}]/[\mathrm{O\ II}])$. Open symbols represent galaxies added data from the *CfA* sample. The best fit slopes for the Sy 1's and Sy 2's are identical; Sy 1: 0.44 ± 0.12 (red line), Sy 2: 0.44 ± 0.22 (blue line). The best fit to the SDSS data is $y = (0.33 \pm 0.004)x - (0.64 \pm 0.08)$. The theoretical reddening vector, derived from Cardelli et al. (1989), is arbitrarily offset for clarity. Our Sy 1 and Sy 2 galaxies are plotted with red triangles and blue squares, respectively, with typical uncertainty shown by the black error bar. The large number of (135,116) of SDSS DR7 galaxies with strong emission-lines (of any origin–AGN or starburst) are plotted as a cloud of light green/gray dots.
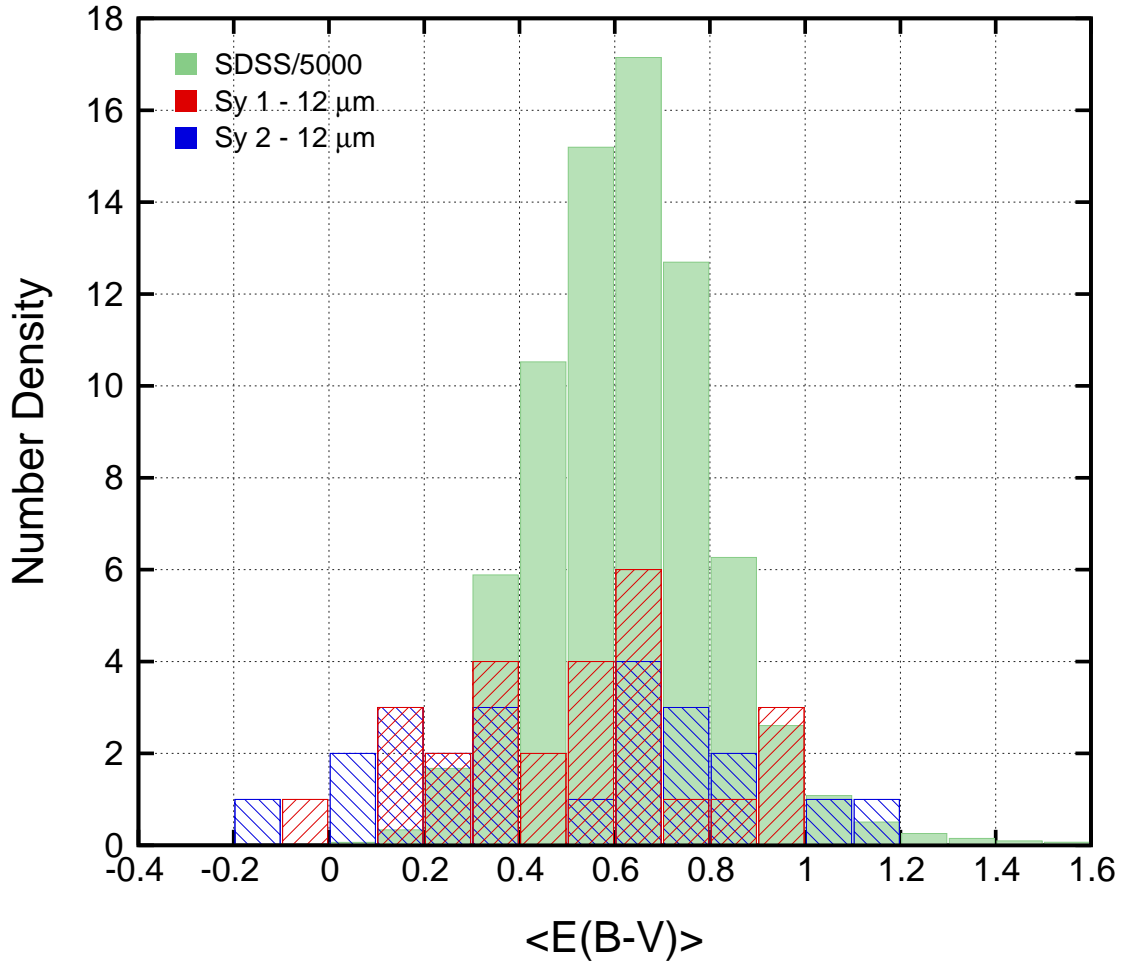
Fig. 3.— Histogram of the average E(B-V) using $H\alpha/H\beta$ and [S II]/[O II] line ratios for the 12 μm Seyferts and the SDSS galaxies. The average reddening is essentially the same in both Seyfert types: $< E(B-V) >= 0.49 \pm 0.35$ for the Sy1's, and $< E(B-V) >= 0.52 \pm 0.26$ for the Sy2's. The average reddening for the SDSS galaxies is $< E(B-V) >= 0.63 \pm 0.21$.
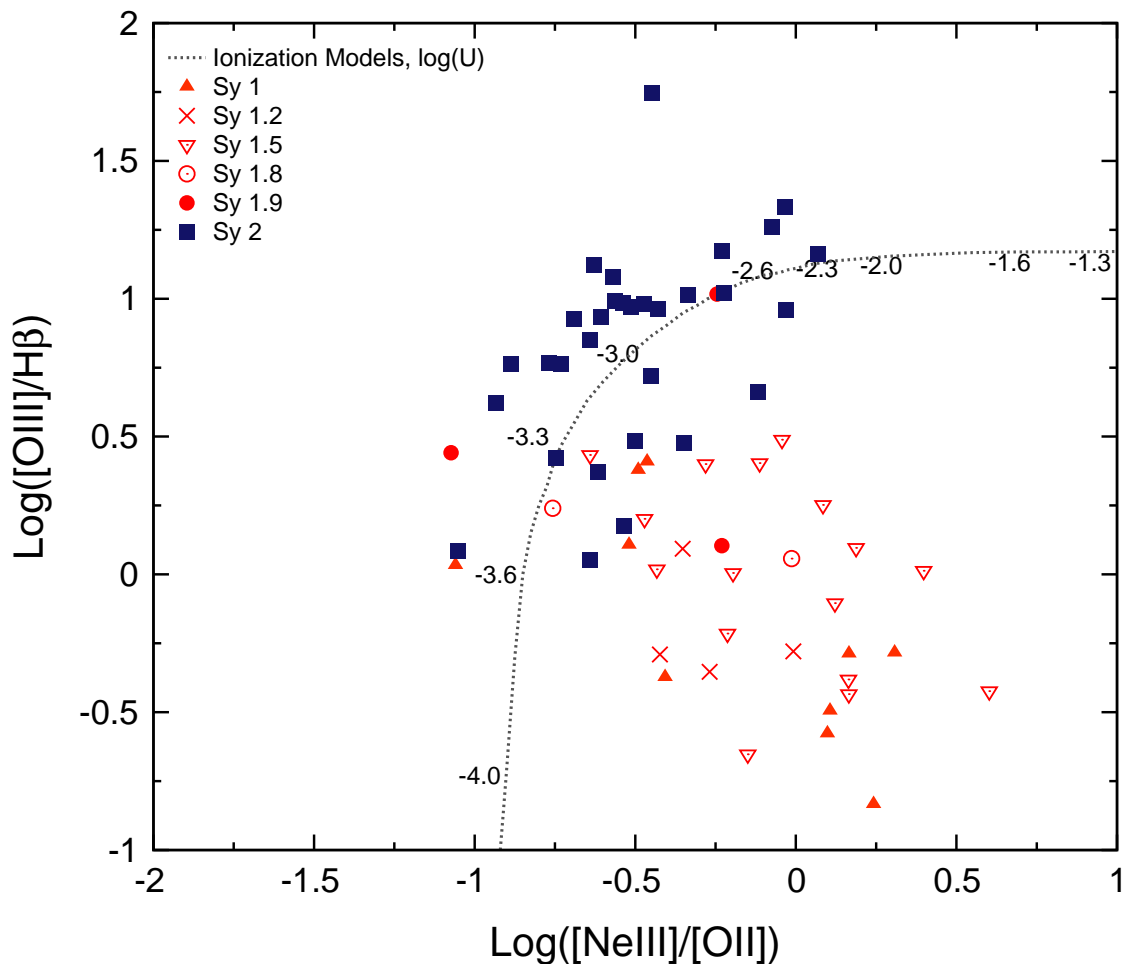
Fig. 4.— Logarithmic line ratios of [O III]/Hβ vs. [Ne III]/[O II]. The dashed line is a sequence of models for the narrow line region from Groves et al. (2004) with the numbers along the line indicating the ionization parameter $U = S_\star/(nc)$, where $S_\star$ is the flux of ionizing photons and n is the number density of hydrogen atoms. Since this model only includes the NLR, most of the Sy 1 galaxies, especially Seyfert 1, 1.2, and 1.5's, falls in the lower right section of the graph, because of their additional $H\beta$ contribution from the BLR.
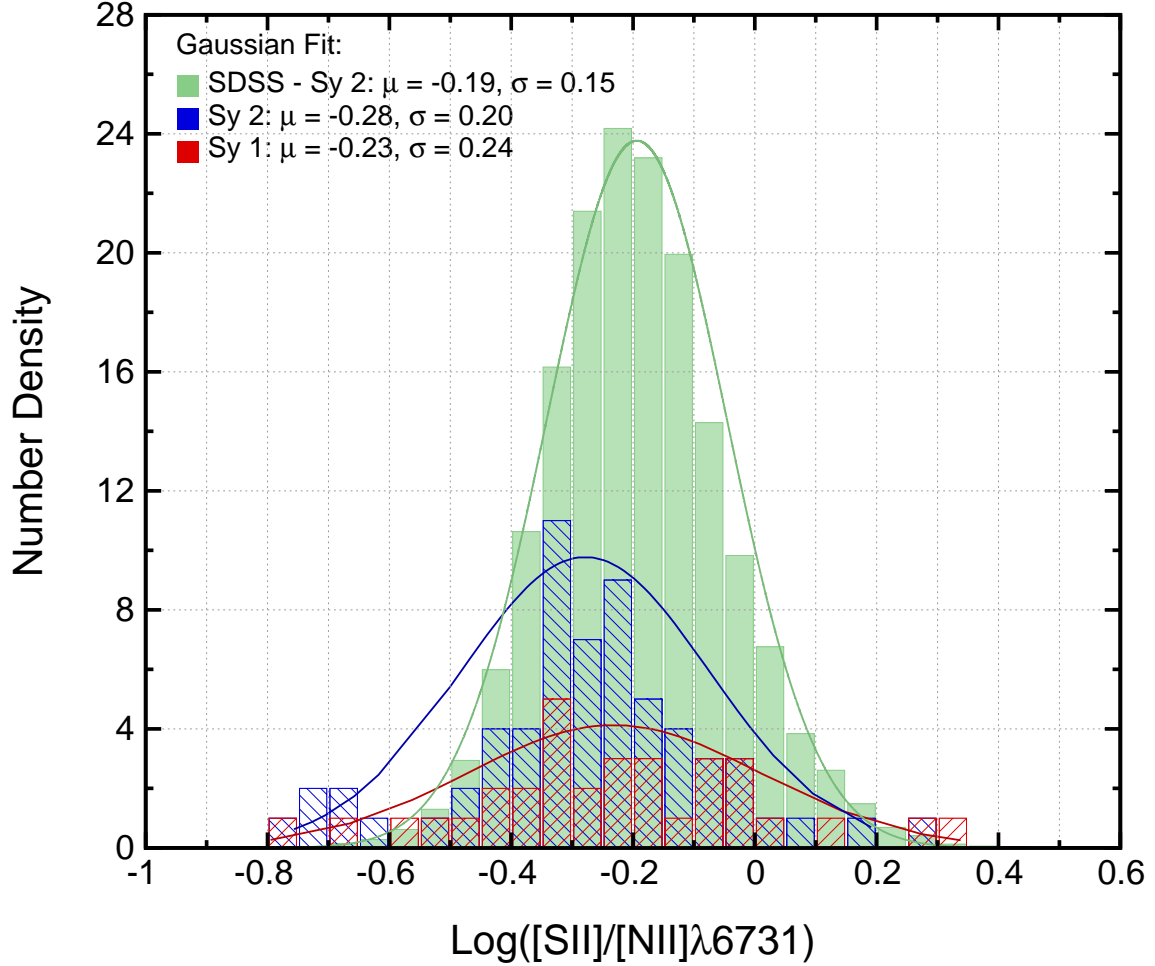
Fig. 5.— Histogram of [S II]/[N II] line raions for our 12 μm Seyfert 1 and Seyfert 2 galaxies (red and blue hatching, respectively). These distributions are quite similar to the line ratios observed in our SDSS DR7 sample of 16,708 Sy 2 galaxies, shown in light green. Each of these distributions can be fitted approximately by a Gaussian. The mean and standard deviation values are given. All of the distributions overlap substaintially, justifying our adoption of a fairly "universal" of log([S II]/[N II])= -0.23. The histogram widths are likely to be dominated by observational uncertainties.
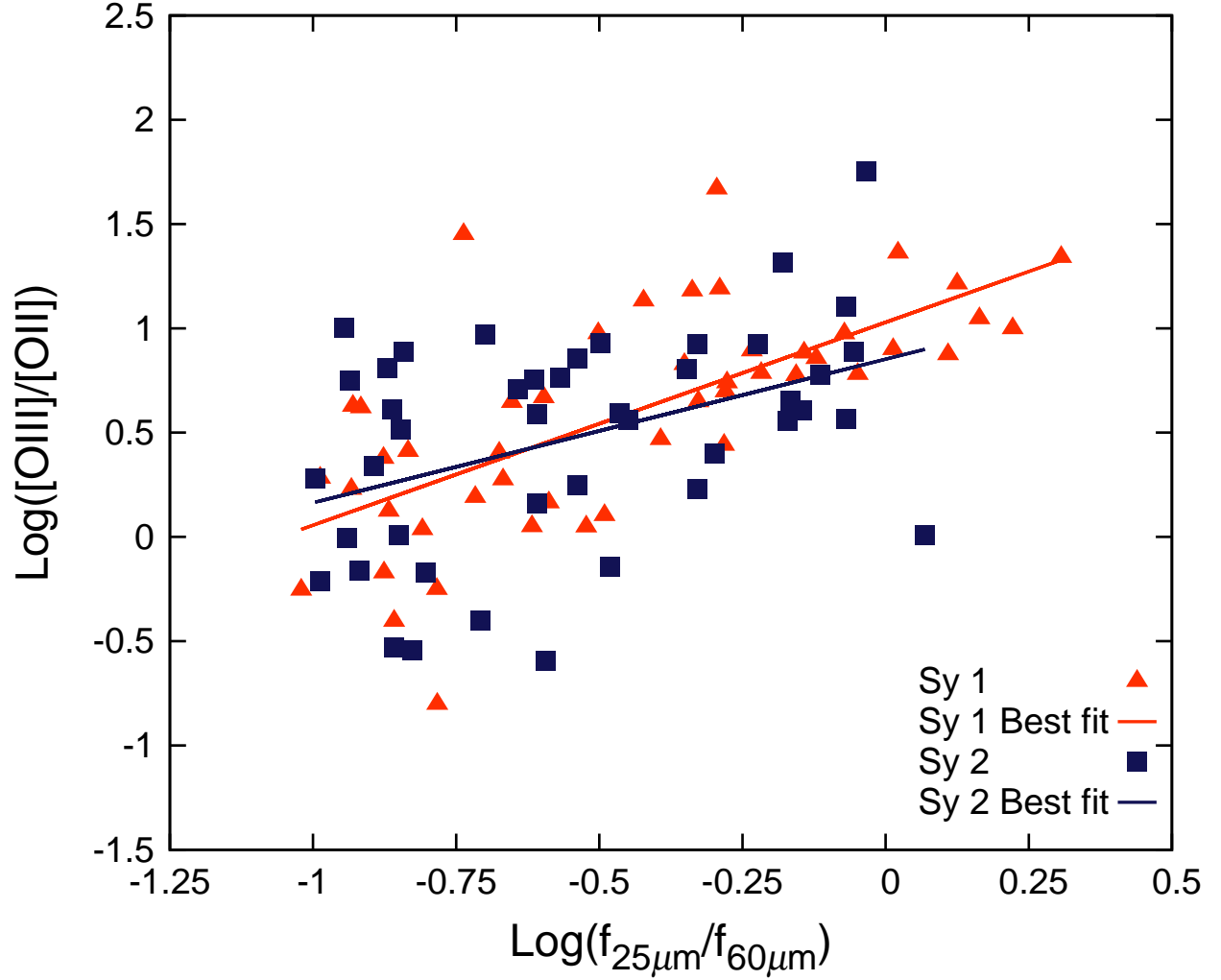
Fig. 6.— Logarithmic line-ratios [O III]/[O II] vs. $f_{25\mu m}/f_{60\mu m}$, which both measure the relative Seyfert nucleus power, compared with the lower-ionization gas and the cooler dust in HII regions. Although this positive correlation shows large scatter, it is significant, with a Sy 1 regression fit of $\log([\text{O III}]/[\text{O II}]) = (0.97 \pm 0.12)\log(f_{25\mu m}/f_{60\mu m}) + (1.03 \pm 0.63)$ and $\log([\text{O III}]/[\text{O II}]) = (0.69 \pm 0.16)\log(f_{25\mu m}/f_{60\mu m}) + (0.85 \pm 0.76)$ for Sy 2 types. A Kendall's Tau significant test confirms that the gas ionization/dust temperature correlation holds for both Sy 1's and Sy 2's, at a CL > 97.5%.
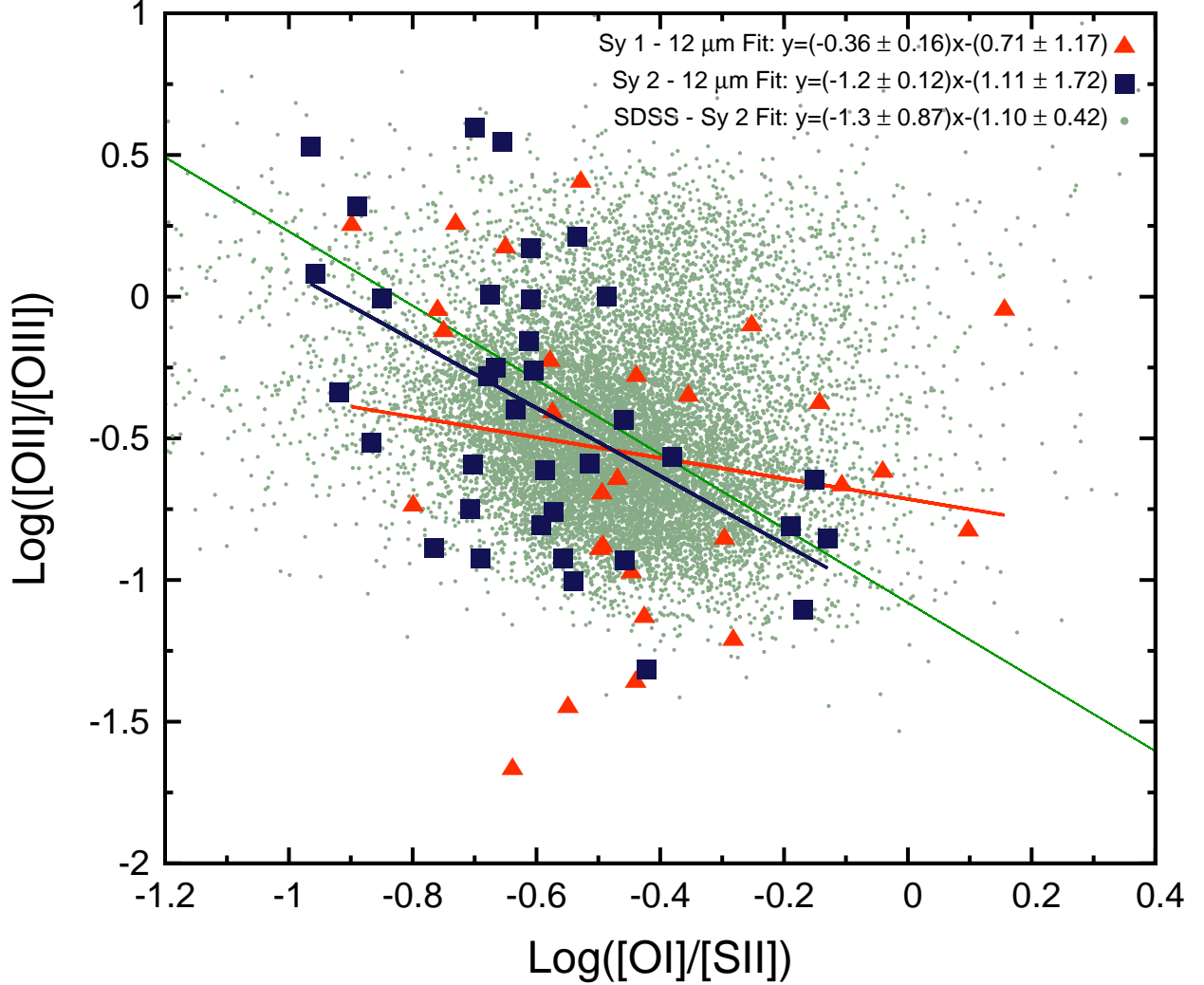
Fig. 7.— Correlation of log([O II]/[O III]) vs. log([O I]/[S II]). We again show our Sy 1 and Sy 2 galaxies as red triangles and blue squares, respectively. The light green/grey points is a subsample of 13,688 Seyfert 2 galaxies from the DR7 of the SDSS. The inverse correlation is the opposite of an ionization effect, and indicates that [O I] follows [O III] more closely than [S II]. This implies that the [O I] emission comes predominantly from the Seyfert nucleus, not from HII regions. The Kendall's Tau significant test reveals that it is significant for the Sy 2 galaxies but not for the Sy 1's, CL = 99.9% and CL < 90% respectively. The slope of the Sy 2 fit is -1.2 ± 0.12 and the slope for the SDSS fit is -1.3 ± 0.87.
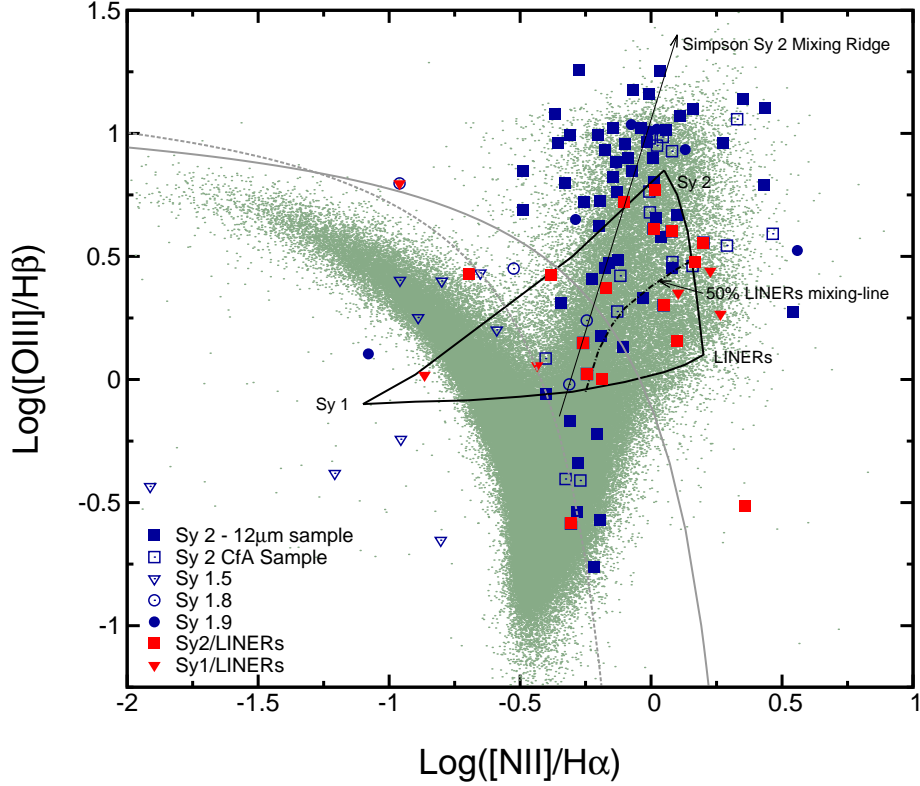
Fig. 8.— BPT line-ratio diagram of our Sy 1.5, 1.8, 1.9, and Sy 2 galaxies, shown by the same color symbols as before. The green/grey dots represent the data form emission-line galaxies from SDSS DR7. We include the boundaries separating AGN and SFG/HII regions from Kauffmann et al. (2003)) (dashed light-grey) and Kewley et al. (2001) (solid light-grey). Most of the Sy 2's fall in the upper right corner as expected, as do Sy 1.9 's. Because of their BLR contimination of the H line-fluxes, the Sy 1.8's fall in the SFR/AGN "composite' region of the BPT diagram, while the Sy 1.5's scatter below the HII/AGN boundary. The mixture of the pure Sy 2 line emmision and HII regions seen in our 12 μm Seyferts are well matched by the Sy 2 "ridge line" from Simpson (2005). The three vertices of the black triangle show our adopted line rations for pure "NLR" (Sy 2, upper right), "BLR" (Sy 1, lower left), and "LINERs" (lower right). The curved line inside the triangle shows a 50% mix of LINER emissions and Seyfert lines. This curve corresponds closely to the boundary between Seyfert 2 (above) and LINER (below) galaxies.
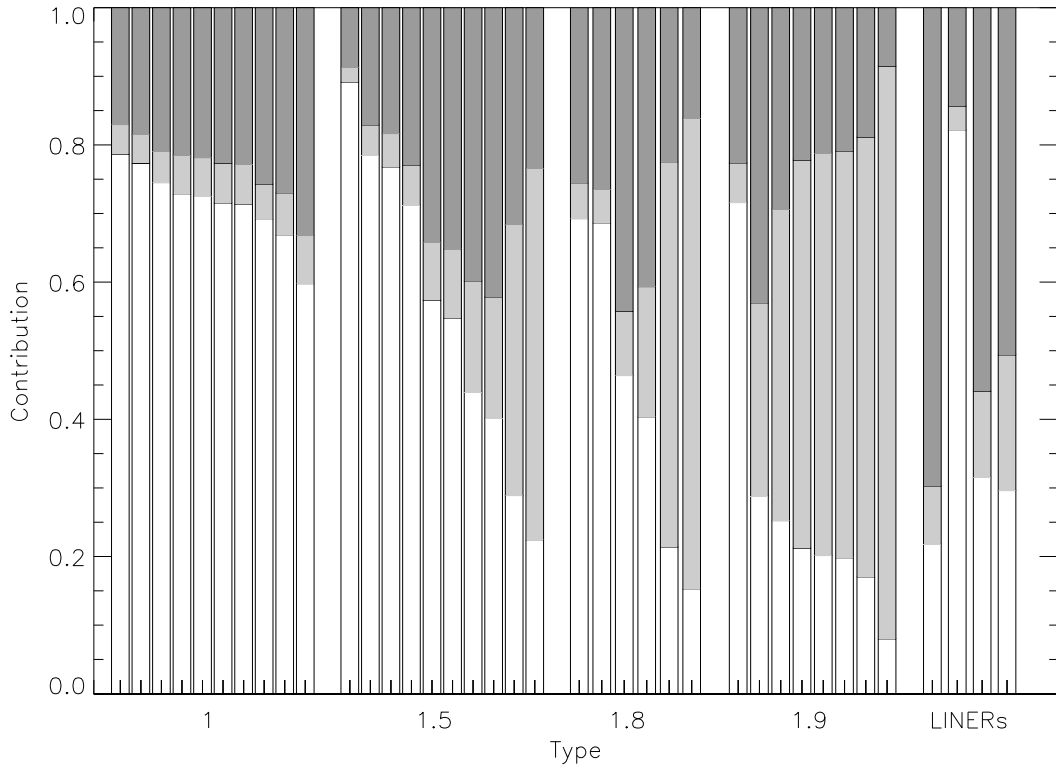
Fig. 9.— Emisson line components of 12 μm of Seyfert 1 galaxies based on their locations in the BPT diagram. White corresponds to the Seyfert 1 contribution, the light gray corresponds to the Seyfert 2 contribution, and the dark gray corresponds to LINER. AGN components classified as Sy 1.8 and 1.9 are dominated by the narrow line component as in the Sy 2's, while the Sy 1.5's are a mix of the Sy 1 and the Sy 2 line components. Spectroscopically classified LINERs have 50% or more of the emission from the LINER component.
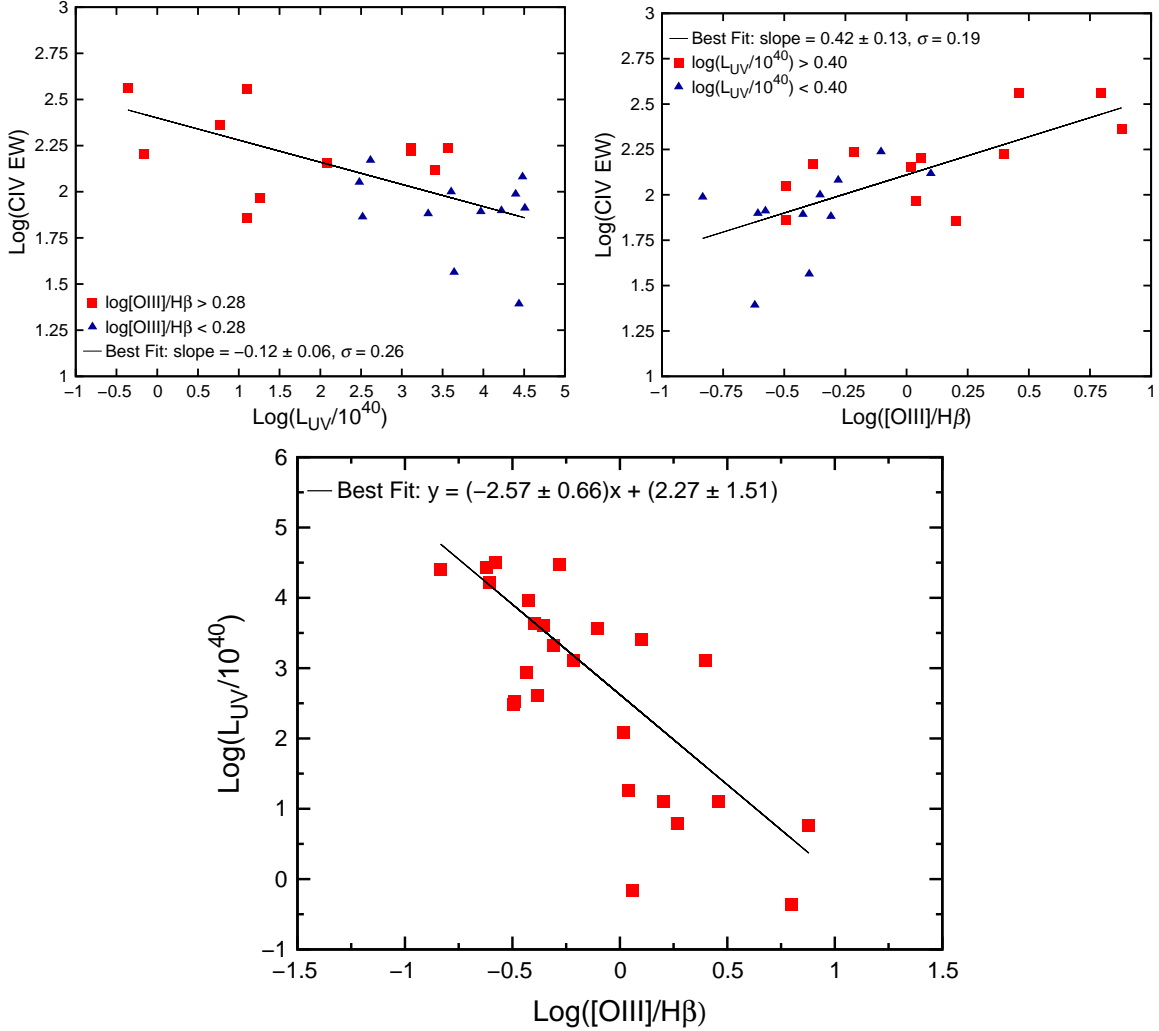
Fig. 10.— *Top Panels*: The classical Baldwin effect is displayed in the left panel and our "substitute Baldwin relation" is shown in the right panel. The symbols for each 12 μm Seyfert 1 are coded by the strength of [O III]/Hβ ratio (left) and $L_{UV}/10^{40}$ (right). The strong segregation between the red and blue points in the left uppper panel indicates that [O III]/Hβ is a good predictor of EW(C IV). The classical Baldwin effect is weak, compared to log(C IV EW) vs. log([O III]/Hβ) (right). The EW(CIV) is much better predicted from log([O III]/Hβ). The $L_{UV}/10^{40}$ parameter hardly improves this. *Bottom Panel*: The strong anticorrelation between log $L_{UV}/10^{40}$ and log([O III]/Hβ) suggests that the classical Baldwin relation is a secondary effect, resulting from this correlation.
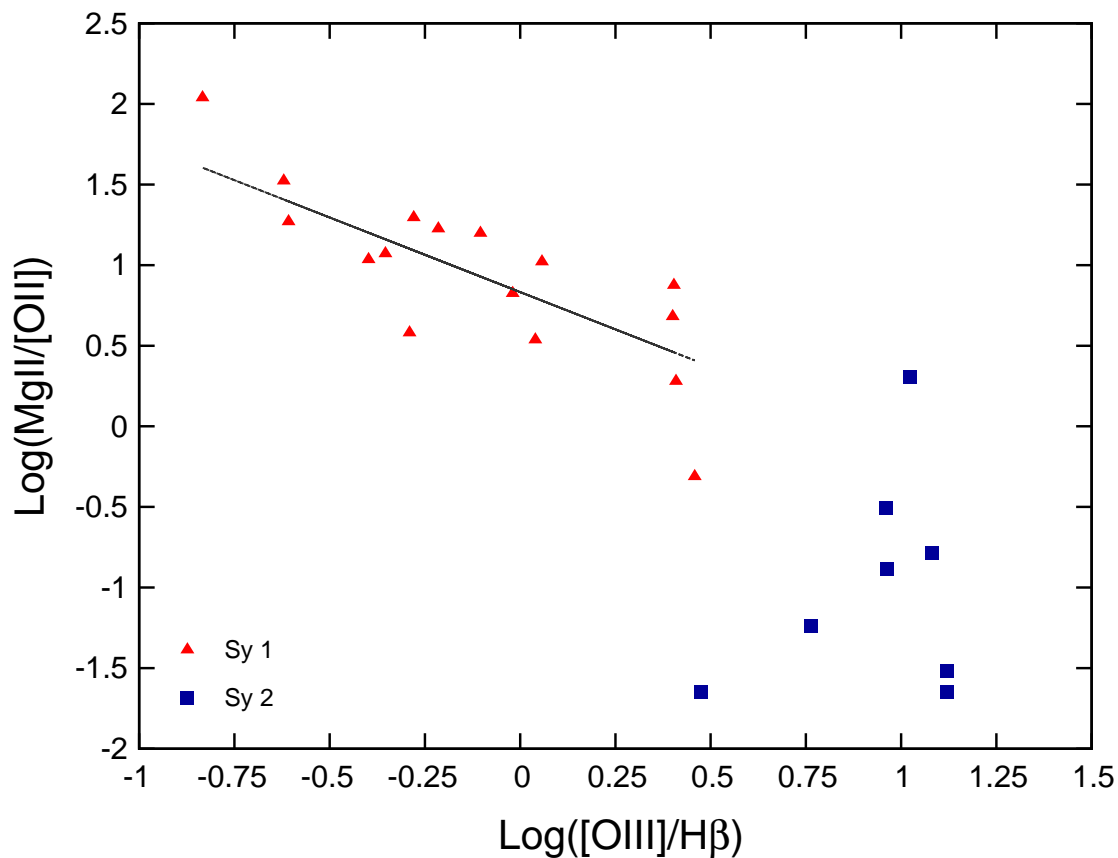
Fig. 11.— Plot of Mg II/[O II] vs. [O III]/Hβ. The best fitting line for the Sy 1 galaxies (red triangles) is log(Mg II/[O II])=(-0.93 ± 0.12)log([O III]/$H\beta$) + 0.84 $\pm$ 0.32. We use [O III]/Hβ as a proxy for weak Fe II (Eigenvector 1), so an inverse correlation for the Sy 1's implies that Mg II and Fe II are correlated. The Seyfert 2 galaxies (blue squares) have no BLR and therefore have much lower Mg II/[O II], and higher [O II]/Hβ ratios.
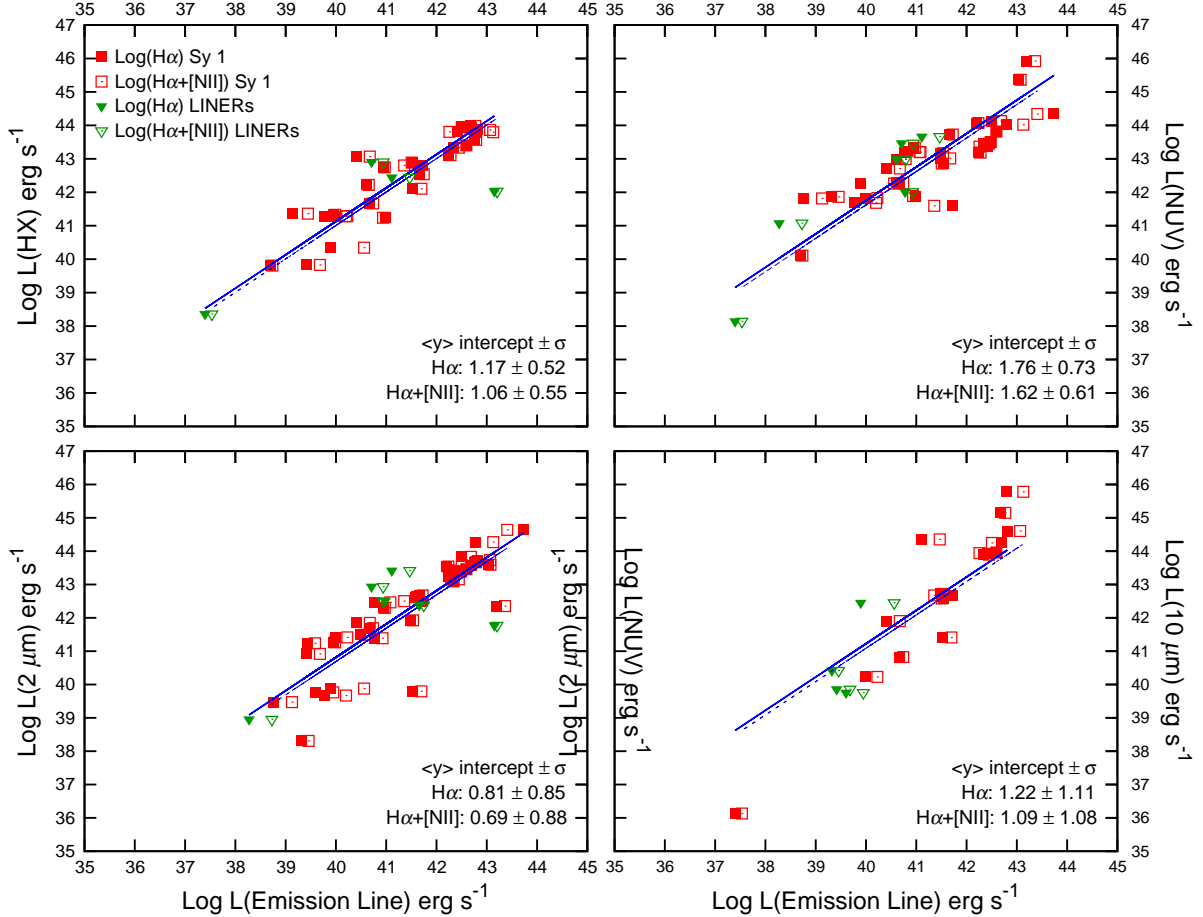
Fig. 12.— Correlation of non-stellar continuum luminosity with emission line luminosity, either with Hα (filled in squares) or with Hα+[N II] (open squares), for Seyfert 1 galaxies. The filled and open triangles (in green) show observations of 12 μm Sy1's which were also classified as either LINERs or Starbursts. The plotted lines are fits of $\log(L_{Continuum}) = A\log(L_{Emission\ Line}) + B$ with a fixed slope of $A = 1$. The tightest correlation is for the HX luminosities, with $L_{HX} \sim 15L_{H\alpha}$ for the Sy 1's and $L_{HX} \sim 11.5L_{(H\alpha+[NII])}$, independent of Seyfert type. Those Sy 1 which have secondary classification as LINERs or Starbursts are expected to harbor relative fainter Syfert nuclei. Nonetheless, they do not deviate systematically from the correlation defined by the more AGN-dominated Sy 1's line/continuum.
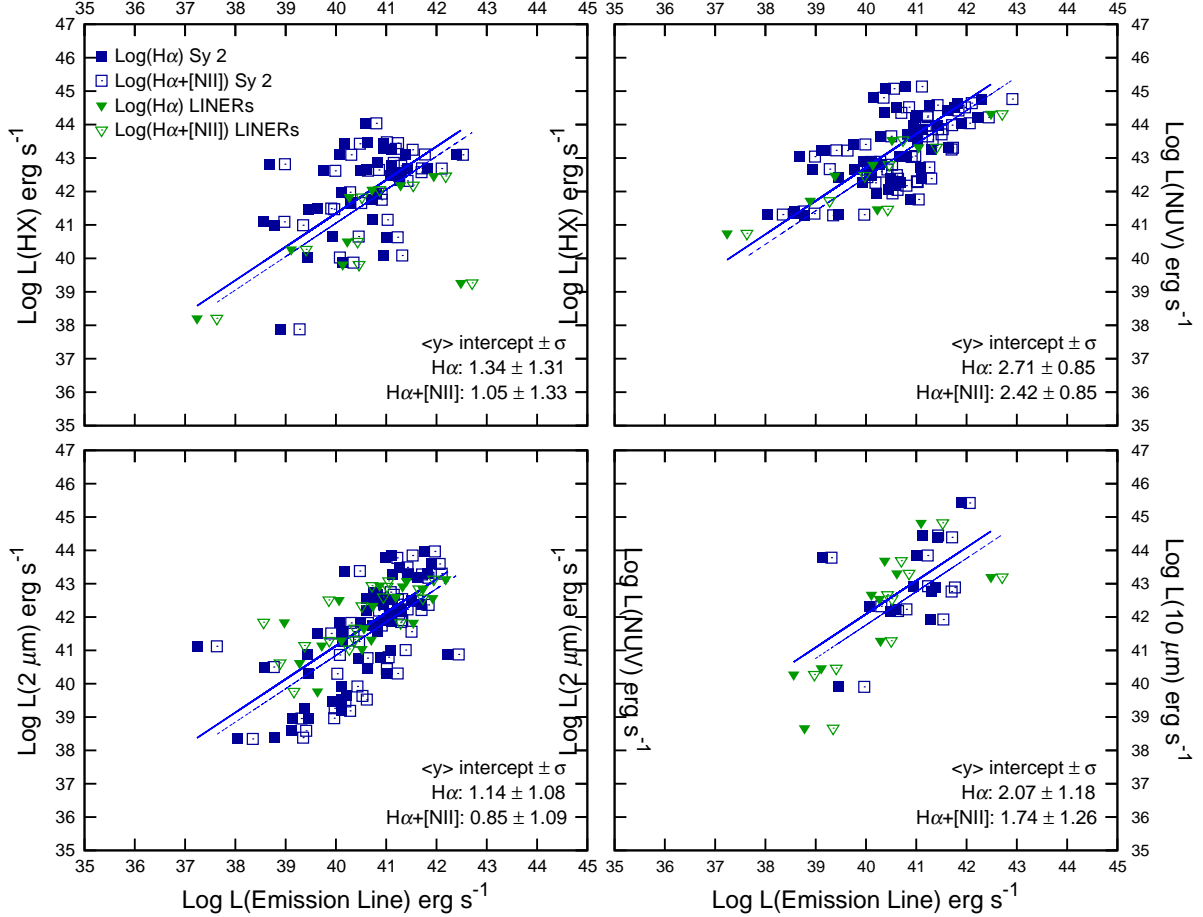
Fig. 13.— Same non-stellar continuum/emission line correlation as shown in Figure 12, except the Seyfert 2 galaxies. The tightest correlation is for the HX luminosities, with $L_{HX} \sim 22 L_{H\alpha}$ for the Sy 2's and $L_{HX} \sim 11.5 L_{(H\alpha+[NII])}$, independent of Seyfert type.
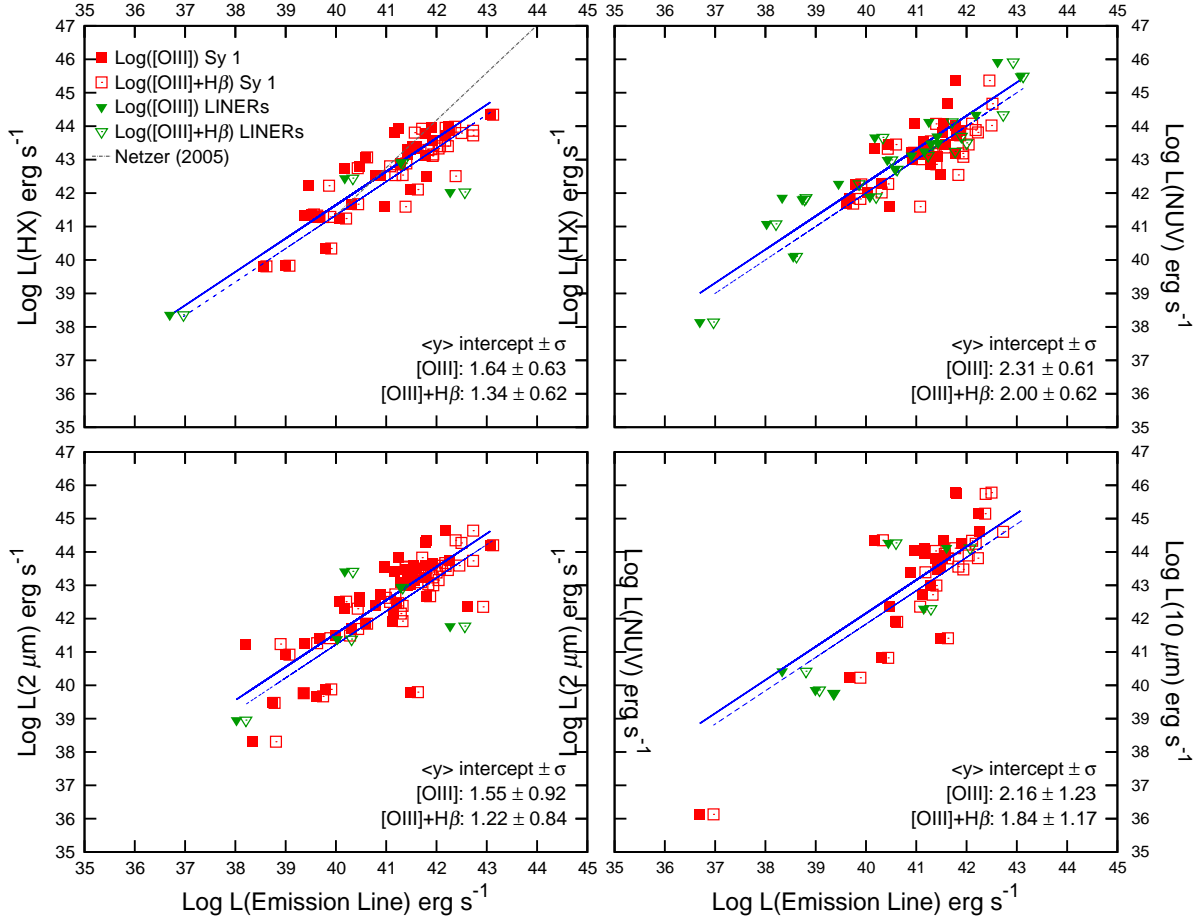
Fig. 14.— Same non-stellar continuum/emission line correlation as shown in Figure 12, but for [O III] and [O III]+Hβ on the x-axis, for Seyfert 1 galaxies. The plotted lines are fits of $\log(L_{Continuum}) = A\log(L_{Emission\ Line}) + B$ with a fixed slope of $A = 1$. The best correlation is for the HX luminosities, with a single relation of $L_{HX} \sim 25L_{([OIII]+H\beta)}$, and with $L_{HX} \sim 44L_{[OIII]}$. The non-linear relation between the L_{HX} and $L_{(Emission\ Line)}$ found by Netzer (2006) is indicated by the steep solid line in the upper left panel.
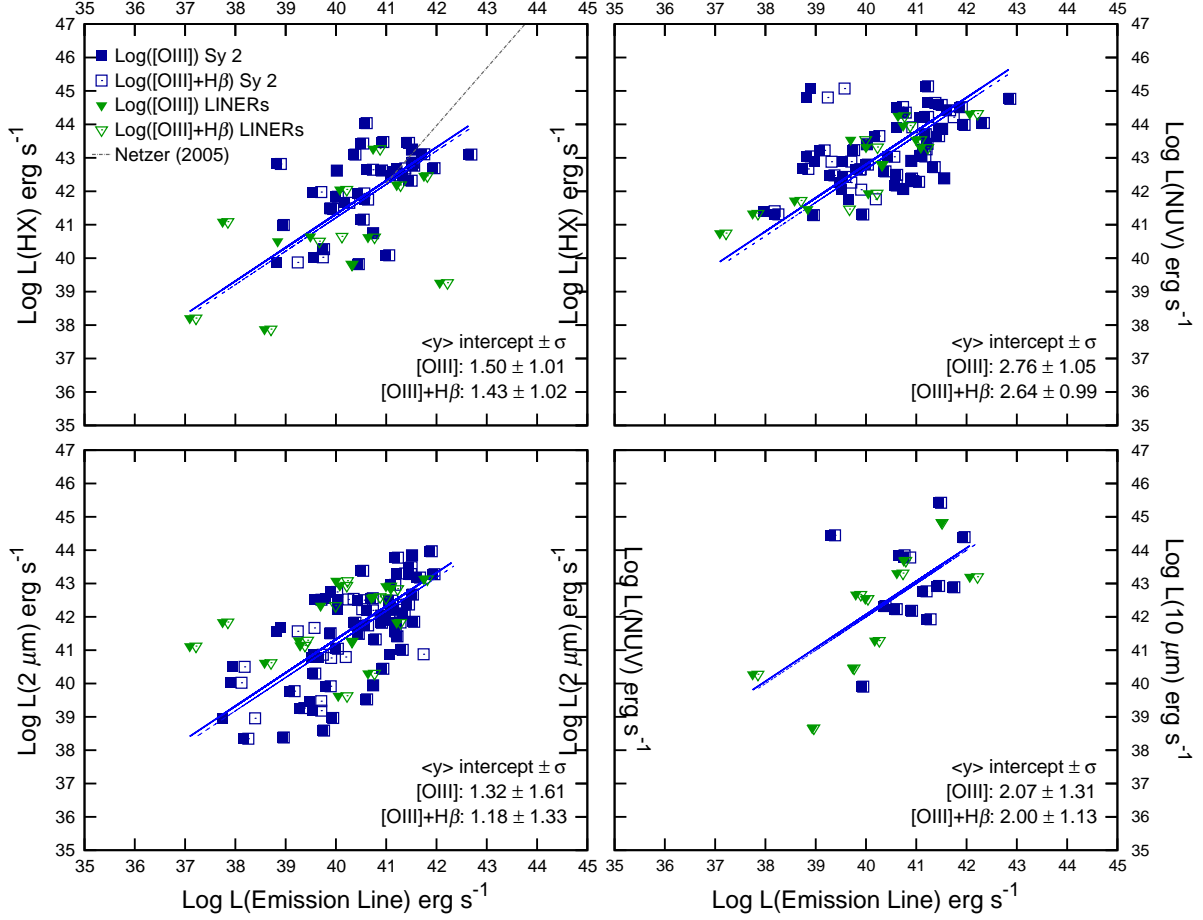
Fig. 15.— Same non-stellar continuum/emission line correlation as shown in Figure 12, but for [O III] and [O III]+Hβ, for Seyfert 2 galaxies. The best correlation is for the HX luminosities, with a single relation of $L_{HX} \sim 25L_{([OIII]+H\beta)}$, and $L_{HX} \sim 32L_{[OIII]}$. The steep solid line in the upper left panel is the same as in Figure 14.

Table 1.   Seyfert 1 Galaxies

Name of Galaxy	RA (J2000)	DEC (J2000)	CfA[a]	Type[b]	Redshift (z)
MKN 334	00h03m09.62s	+21d57m36.6s	∗	1.8	0.022
MKN 335	00h06m19.52s	+20d12m10.5s		1.2	0.026
ESO 540-G1	00h34m13.82s	-21d26m20.6s		1.8	0.027
ESO 12-G21	00h40m46.26s	-79d14m24.2s		1	0.030
IRAS 00488+2907	00h51m35.01s	+29d24m04.5s	∗	1	0.036
I ZW 1	00h53m34.94s	+12d41m36.2s		1/STBRST	0.061
NGC 526A	01h23m54.39s	-35d03m55.9s	∗	1.5	0.019
MKN 993	01h25m31.46s	+32d08m11.4s	∗	1.5	0.016
IRAS 01527+0622	01h55m22.04s	+06d36m42.6s	∗	1.9	0.017
MKN 590	02h14m33.56s	-00d46m00.1s	∗	1.2	0.026
MKN 1034	02h23m20.45s	+32d11m34.2s		1	0.034
M-3-7-11	02h24m40.62s	-19d08m31.3s		1.8	0.034
NGC 931	02h28m14.48s	+31d18m42.0s		1.5	0.017
NGC 1097	02h46m19.05s	-30d16m29.6s		1	0.004
NGC 1365	03h33m36.37s	-36d08m25.4s		1.8	0.005
IRAS F03450+0055	03h47m40.19s	+01d05m14.0s		1	0.031
NGC 1566	04h20m00.42s	-54d56m16.1s		1	0.005
3C 120	04h33m11.10s	+05d21m15.6s		1	0.033
MKN 618	04h36m22.24s	-10d22m33.8s		1	0.036
M-5-13-17	05h19m35.80s	-32d39m27.3s		1.5	0.012
IRAS F05563-3820	05h58m02.00s	-38d20m04.7s		1	0.034
MKN 6	06h52m12.25s	+74d25m37.5s		1.5	0.019
MKN 9	07h36m56.98s	+58d46m13.4s		1.5	0.040
MKN 79	07h42m32.80s	+49d48m34.7s		1.2	0.022
IRAS F07599+6508	08h04m33.08s	+64d59m48.6s		1	0.148
NGC 2639	08h43m38.08s	+50d12m20.0s		1.9	0.011
NGC 2782	09h14m05.11s	+40d06m49.3s	∗	1/STBRST	0.008
MKN 704	09h18m26.01s	+16d18m19.2s		1.5	0.029
NGC 2841	09h22m02.63s	+50d58m35.5s	∗	1/LINER	0.002
UCG 5101	09h35m51.60s	+61d21m11.5s		1.5/LINER	0.039
NGC 2992	09h45m42.05s	-14d19m35.0s		1.9	0.008
MKN 1239	09h52m19.10s	-01d36m43.5s		1.5/LINER	0.020
NGC 3031	09h55m33.17s	+69d03m55.1s		1.8	-0.0001
MKN 1243	09h59m55.84s	+13d02m37.8s	∗	1	0.035
3C 234	10h01m49.52s	+28d47m09.0s		1	0.185
NGC 3227	10h23m30.58s	+19d51m54.2s		1.5	0.004
NGC 3511	11h03m23.77s	-23d05m12.4s		1	0.004

Table 1—Continued

Name of Galaxy	RA (J2000)	DEC (J2000)	CfA[a]	Type[b]	Redshift (z)
NGC 3516	11h06m47.49s	+72d34m06.9s		1.5	0.009
MKN 744	11h39m42.55s	+31d54m33.4s	*	1.8	0.009
NGC 4051	12h03m09.61s	+44d31m52.8s		1.5	0.002
UCG 7064	12h04m43.32s	+31d10m38.2s		1.9	0.025
NGC 4151	12h10m32.58s	+39d24m20.6s		1.5	0.003
NGC 4235	12h17m09.88s	+07d11m29.7s	*	1.5	0.008
NGC 4253	12h18m26.51s	+29d48m46.3s		1.5	0.013
MKN 205	12h21m44.22s	+75d18m38.8s	*	1	0.071
NGC 4395	12h25m48.86s	+33d32m48.9s	*	1.8/LINER	0.001
3C 273	12h29m06.70s	+02d03m08.6s		1	0.158
NGC 4565	12h36m20.78s	+25d59m15.6s	*	1.9	0.004
NGC 4579	12h37m43.52s	+11d49m05.5s		1.9/LINER	0.005
NGC 4593	12h39m39.43s	-05d20m39.3s		1	0.009
NGC 4594	12h39m59.43s	-11d37m23.0s		1.9/LINER	0.003
NGC 4602	12h40m36.85s	-05d07m58.8s		1.9	0.008
M-2-33-34	12h52m12.46s	-13d24m53.0s		1	0.015
MKN 231	12h56m14.23s	+56d52m25.2s		1	0.042
NGC 5033	13h13m27.47s	+36d35m38.2s		1.9	0.003
M-6-30-15	13h35m53.71s	-34d17m43.9s		1.2	0.008
IRAS F13349+2438	13h37m18.73s	+24d23m03.4s		1	0.108
IRAS 13354+3924	13h37m39.87s	+39d09m17.0s	*	1.8	0.020
NGC 5252	13h38m15.96s	+04d32m33.3s	*	1.9	0.023
NGC 5273	13h42m08.34s	+35d39m15.2s	*	1.9	0.004
IC 4329A	13h49m19.27s	-30d18m34.0s		1.2	0.016
MKN 279	13h53m03.45s	+69d18m29.6s	*	1.5	0.030
NGC 5548	14h17m59.53s	+25d08m12.4s		1.5	0.017
MKN 471	14h22m55.37s	+32d51m02.7s	*	1.8	0.034
NGC 5674	14h33m52.24s	+05d27m29.6s	*	1.9	0.025
MKN 817	14h36m22.07s	+58d47m39.4s		1.5	0.031
MKN 841	15h04m01.20s	+10d26m16.2s	*	1.5	0.036
IRAS F15091-2107	15h11m59.80s	-21d19m01.7s		1	0.045
NGC 5905	15h15m23.32s	+55d31m02.5s		1	0.011
CGCG 022-021	15h38m44.74s	-03d22m48.2s	*	1.9	0.024
IRAS 16146+3549	16h16m30.69s	+35d42m29.0s	*	1.5	0.028
ESO 141-G55	19h21m14.14s	-58d40m13.1s		1	0.036
NGC 6860	20h08m46.89s	-61d06m00.7s		1	0.015
MKN 509	20h44m09.74s	-10d43m24.5s		1.2	0.034

Table 1—Continued

Name of Galaxy	RA (J2000)	DEC (J2000)	CfA[a]	Type[b]	Redshift (z)
NGC 7213	22h09m16.31s	-47d09m59.8s		1.5/LINER	0.006
ESO 344-G16	22h14m42.01s	-38d48m22.9s		1.5	0.040
3C 445	22h23m49.53s	-02d06m12.9s		1	0.056
NGC 7314	22h35m46.19s	-26d03m01.7s		1.9	0.005
UGC 12138	22h40m17.05s	+08d03m14.1s	∗	1.8	0.025
NGC 7469	23h03m15.62s	+08d52m26.4s		1.2	0.016
NGC 7603	23h18m56.62s	+00d14m38.2s		1.5	0.030

[a]An asterisk marks if this object was added from the CfA sample.

[b]As listed under 'BASIC DATA - Classifications' in Nasa/Ipac Extragalactic Database (NED), https://ned.ipac.caltech.edu.

Note. — This Table, as are all the data tables, are sorted by increasing RA starting with the Seyfert 1's then doing the same for the Seyfert 2's.

Table 2.   Seyfert 2 Galaxies

Name of Galaxy	RA (J2000)	DEC (J2000)	CfA[a]	Type[b]	Redshift (z)
NGC 34	00h11m06.55s	-12d06m26.3s		2	0.020
IRAS F00198-7926	00h21m53.61s	-79d10m07.5s		2	0.073
NGC 262	00h48m47.14s	+31d57m25.1s		2	0.015
IRAS F00521-7054	00h53m56.15s	-70d38m04.2s		2	0.069
ESO 541-IG12	01h02m17.55s	-19d40m08.7s		2	0.057
NGC 424	01h11m27.63s	-38d05m00.5s		2	0.012
NGC 513	01h24m26.85s	+33d47m58.0s		2	0.020
MKN 573	01h43m57.80s	+02d20m59.7s	∗	2	0.017
IRAS F01475-0740	01h50m02.70s	-07d25m48.5s		2	0.018
NGC 833	02h09m20.84s	-10d07m59.1s	∗	2/LINER	0.013
NGC 839	02h09m42.93s	-10d11m02.7s		2/LINER	0.013
UGC 2024	02h33m01.24s	+00d25m15.0s		2	0.022
NGC 1052	02h41m04.80s	-08d15m20.8s	∗	2/LINER	0.005
NGC 1068	02h42m40.71s	-00d00m47.8s		2	0.004
NGC 1125	02h51m40.27s	-16d39m03.7s		2	0.011
NGC 1144/1143	02h55m12.2s	-00d11m01s		2	0.029
M-2-8-39	03h00m30.59s	-11d24m56.6s		2	0.030
NGC 1194	03h03m49.11s	-01d06m13.5s		2	0.014
NGC 1241	03h11m14.64s	-08d55m19.7s		2	0.014
NGC 1320	03h24m48.70s	-03d02m32.2s		2	0.009
NGC 1386	03h36m46.18s	-35d59m57.9s		2	0.003
IRAS F03362-1642	03h38m33.58s	-16d32m15.6s		2	0.037
NGC 1433	03h42m01.55s	-47d13m19.5s		2	0.004
ESO 420-G13	04h13m49.69s	-32d00m25.1s	∗	2	0.012
IRAS 04259-0440	04h28m26.05s	-04d33m49.5s	∗	2/LINER	0.016
NGC 1614	04h33m59.85s	-08d34m44.0s	∗	2/STBRST	0.016
NGC 1667	04h48m37.14s	-06d19m11.9s	∗	2	0.015
NGC 1672	04h45m42.50s	-59d14m49.9s	∗	2	0.004
ESO 033-G002	04h55m58.96s	-75d32m28.2s		2	0.018
NGC 1808	05h07m42.34s	-37d30m47.0s		2	0.003
IRAS F05189-2524	05h21m01.39s	-25d21m45.4s		2	0.043
NGC 2655	08h55m37.73s	+78d13m23.1s	∗	2	0.005
NGC 2683	08h52m41.33s	+33d25m18.3s		2/LINER	0.001
IRAS F08572+3915	09h00m25.39s	+39d03m54.4s		2/LINER	0.058
NGC 3079	10h01m57.80s	+55d40m47.2s	∗	2/LINER	0.004
NGC 3147	10h16m53.65s	+73d24m02.7s		2	0.009
NGC 3362	10h44m51.72s	+06d35m48.2s	∗	2	0.028

Table 2—Continued

Name of Galaxy	RA (J2000)	DEC (J2000)	CfA[a]	Type[b]	Redshift (z)
NGC 3486	11h00m23.87s	+28d58m30.5s		2	0.002
UCG 6100	11h01m34.00s	+45d39m14.2s	∗	2	0.030
NGC 3593	11h14m37.00s	+12d49m03.6s	∗	2/LINER	0.002
NGC 3627	11h20m14.96s	+12d59m29.5s	∗	2	0.002
M 0-29-23	11h21m12.26s	-02d59m03.5s		2	0.025
NGC 3660	11h23m32.28s	-08d39m30.8s		2	0.012
NGC 3735	11h35m57.30s	+70d32m08.1s	∗	2	0.009
NGC 3822	11h42m11.11s	+10d16m40.0s		2	0.020
NGC 3976	11h55m57.29s	+06d44m58.0s	∗	2	0.008
NGC 3982	11h56m28.13s	+55d07m30.9s		2	0.004
NGC 4303	12h21m54.90s	+04d28m25.1s		2	0.005
NGC 4388	12h25m46.75s	+12d39m43.5s		2	0.008
IC 3639	12h40m52.85s	-36d45m21.1s		2	0.011
NGC 4628	12h42m25.26s	-06d58m15.6s	∗	2	0.009
NGC 4826	12h56m43.64s	+21d40m58.7s		2	0.001
NGC 4922	13h01m24.90s	+29d18m40.0s		2/LINER	0.024
NGC 4941	13h04m13.14s	-05d33m05.8s		2	0.004
NGC 4968	13h07m05.98s	-23d40m37.3s		2	0.010
NGC 5005	13h10m56.23s	+37d03m33.1s		2/LINER	0.003
M-3-34-64	13h22m24.46s	-16d43m42.5s		2	0.017
NGC 5135	13h25m44.06s	-29d50m01.2s		2	0.014
NGC 5194	13h29m52.71s	+47d11m42.6s		2	0.002
NGC 5248	13h37m32.02s	+08d53m06.6s		2	0.004
NGC 5256	13h38m17.50s	+48d16m37.0s	∗	2/STBRST	0.028
MKN 270	13h41m05.76s	+67d40m20.3s	∗	2	0.010
NGC 5278	13h41m39.62s	+55d40m14.3s		2	0.025
MKN 273	13h44m42.11s	+55d53m12.7s		2/LINER	0.038
MKN 796	13h46m49.45s	+14d24m01.7s	∗	2	0.022
MKN 1361	13h47m04.36s	+11d06m22.6s		2	0.023
MKN 461	13h47m17.75s	+34d08m55.7s	∗	2	0.016
NGC 5347	13h53m17.83s	+33d29m27.0s		2	0.008
MKN 463	13h56m02.87s	+18d22m19.5s		2	0.050
NGC 5395	13h58m37.98s	+37d25m28.1s	∗	2	0.012
NGC 5506	14h13m14.89s	-03d12m27.3s		2	0.006
MKN 686	14h37m22.12s	+36d34m04.1s	∗	2	0.014
NGC 5899	15h15m03.22s	+42d02m59.4s	∗	2	0.009
NGC 5929	15h26m06.16s	+41d40m14.4s	∗	2	0.008

Table 2—Continued

Name of Galaxy	RA (J2000)	DEC (J2000)	CfA[a]	Type[b]	Redshift (z)
NGC 5953	15h34m32.38s	+15d11m37.6s		2/LINER	0.007
UGC 9913	15h34m57.12s	+23d30m11.5s		2/LINER	0.018
UGC 9944	15h35m47.86s	+73d27m02.5s	∗	2	0.025
NGC 5995	15h48m24.95s	-13d45m28.0s		2	0.025
IRAS F15480-0344	15h50m41.50s	-03d53m18.3s		2	0.030
NGC 6217	16h32m39.20s	+78d11m53.4s		2	0.005
NGC 6240	16h52m58.87s	+02d24m03.3s		2/LINER	0.024
NGC 6552	18h00m07.23s	+66d36m54.4s	∗	2	0.026
NGC 6810	19h43m34.25s	-58d39m20.1s		2	0.007
ESO 339-G11	19h57m37.58s	-37d56m08.3s		2	0.019
NGC 6890	20h18m18.10s	-44d48m24.2s		2	0.008
IC 5063	20h52m02.34s	-57d04m07.6s		2	0.011
MKN 897	21h07m45.82s	+03d52m40.4s		2	0.026
NGC 7130	21h48m19.52s	-34d57m04.5s		2/LINER	0.016
NGC 7172	22h02m01.89s	-31d52m10.8s	∗	2	0.009
IRAS F22017+0319	22h04m19.17s	+03d33m50.2s		2	0.061
IC 5169	22h10m09.98s	-36d05m19.0s		2	0.010
M-3-58-07	22h49m37.15s	-19d16m26.4s		2	0.031
NGC 7479	23h04m56.65s	+12d19m22.4s	∗	2/LINER	0.008
NGC 7496	23h09m47.29s	-43d25m40.6s		2	0.006
ESO 148-IG2	23h15m46.75s	-59d03m15.6s		2/STBRST	0.045
IC 5298	23h16m00.70s	+25d33m24.1s	∗	2/STBRST	0.027
NGC 7582	23h18m23.50s	-42d22m14.0s		2	0.005
NGC 7590	23h18m54.81s	-42d14m20.6s		2	0.005
NGC 7674	23h27m56.72s	+08d46m44.5s		2	0.029
NGC 7678	23h28m27.90s	+22d25m16.3s	∗	2/STBRST	0.012
NGC 7682	23h29m03.93s	+03d32m00.0s	∗	2	0.017
NGC 7733	23h42m32.95s	-65d57m23.4s	∗	2	0.034
CGCG 381-051	23h48m41.72s	02d14m23.1s		2	0.031
MKN 331	23h51m26.80s	+20d35m09.9s	∗	2	0.018

[a]An asterisk marks if this object was added from the CfA sample.

[b]As listed under 'BASIC DATA - Classifications' in Nasa/Ipac Extragalactic Database (NED), https://ned.ipac.caltech.edu.

Note. — This Table, as are all the data tables, are sorted by increasing RA starting with

the Seyfert 1's then doing the same for the Seyfert 2's.

Table 3.   Emission Lines

Emission Line	Wavelength (Å)	Ionization Potential Lower (eV)	Ionization Potential Upper (eV)	Critical Density (cm^{-3})
Lyman α	1216	$\cdots$	13.6	$\cdots$
N V	1240, 1243	77.5	97.9	$\cdots$
C IV	1549, 1551	47.9	64.5	$\cdots$
C III]	1907, 1909	24.4	47.9	1×10^{10}
Mg II	2796, 2804	7.6	15.0	$\cdots$
[Ne V]	3426	97.1	126.2	1.6×10^{7}
[O II]	3727, 3729	13.6	35.1	4.5×10^{3}
[Ne III]	3869	41.0	63.5	9.7×10^{6}
Hβ	4861	$\cdots$	13.6	$\cdots$
[O III]	4959	35.1	54.9	7.0×10^{5}
[O III]	5007	35.1	54.9	7.0×10^{5}
[O I]	6300	$\cdots$	13.6	1.8×10^{6}
[N II]	6549, 6583	14.5	29.6	8.7×10^{4}
Hα	6563	$\cdots$	13.6	$\cdots$
[S II]	6717, 6734	10.4	23.3	1.5×10^{3}, 3.9×10^{3}

Note. — Emission lines and their corresponding wavelength. The ionization potentials and critical densities are from De Robertis & Osterbrock (1986), Morton (2003), Osterbrock & Ferland (2006), and SPECTR-W3 (`http://spectr-w3.snz.ru/ion.phtml`).

Table 4.   Optical Emission Line Data

Name	[NeV][a]	[OII]	[NeIII]	Hβ	[OIII] 4959Å	[OIII] 5007Å	[OI]	Hα	[NII]	Hα + [NII]	[SII]	Ref
Seyfert 1												
MKN 334	0.71	7.03	1.23	4.48	2.38	7.87	1.29	28.35	16.1	$\cdots$	7.42	1,2
MKN 335	6.3	3	11	91	6.3	22.45	$\cdots$	$\cdots$	$\cdots$	264.8	$\cdots$	1,3
E 540-G1	$\cdots$	1.95	$\cdots$	2.71	$\cdots$	2.59	0.4	9.69	4.72	$\cdots$	2.25	4,5
E12-G21	$\cdots$	$\cdots$	$\cdots$	14.8	$\cdots$	9.95	$\cdots$	111	$\cdots$	$\cdots$	$\cdots$	6,7
IRAS 00488+2907	$\cdots$	$\cdots$	$\cdots$	$\cdots$	$\cdots$	$\cdots$	$\cdots$	$\cdots$	$\cdots$	$\cdots$	$\cdots$	
I ZW 1	6.3	2.7	4.3	31	4.6	7.43	$\cdots$	74.8	11	164.8	$\cdots$	1,8
NGC 526A	$\cdots$	11	3.41	2.15	8.4	24.7	1.6	6.44	4.54	$\cdots$	3.62	3,7
MKN 993	$\cdots$	$\cdots$	$\cdots$	1.13	1.02	5.05	0.51	7.71	3.97	$\cdots$	1.81	2,9
IRAS 01527+0622	$\cdots$	$\cdots$	$\cdots$	$\cdots$	$\cdots$	$\cdots$	$\cdots$	$\cdots$	$\cdots$	$\cdots$	$\cdots$	2
MKN 590	$\cdots$	$\cdots$	$\cdots$	6.02	$\cdots$	5.25	$\cdots$	$\cdots$	$\cdots$	170	$\cdots$	3,10
MKN 1034	$\cdots$	0.65	0.21	0.46	0.81	1.1	0.66	$\cdots$	$\cdots$	13.8	2.5	1,11
M-3-7-11	$\cdots$	$\cdots$	$\cdots$	4.5	8.9	25	1.37	18.35	2.56	$\cdots$	4.8	6,12
NGC 931	1.17	0.26	0.65	11.8	3.85	12.13	0.48	$\cdots$	$\cdots$	67.1	2.09	1,3
NGC 1097	$\cdots$	11.1	$\cdots$	10.1	$\cdots$	1.75	$\cdots$	42.4	25.61	$\cdots$	10.83	6,13,14
NGC 1365	$\cdots$	16.6	$\cdots$	6	$\cdots$	18	$\cdots$	143.1	$\cdots$	130	$\cdots$	6,10,15
F03450+0055	$\cdots$	$\cdots$	$\cdots$	21.27	$\cdots$	6.86	0.92	$\cdots$	$\cdots$	114.25	1.42	1,16
NGC 1566	$\cdots$	7.64	3.07	16.6	7.28	18.2	4.19	56.3	12	$\cdots$	5.82	7,25
3C 120	$\cdots$	$\cdots$	3.5	30.4	13.4	38.2	1.5	208.9	10	133.67	$\cdots$	1,6,10,18
MKN 618	3.59	1.49	2.18	27.24	4.8	14.05	0.74	$\cdots$	$\cdots$	118.15	2.07	1,3,10,16
M-5-13-17	$\cdots$	5.43	6.6	20.4	14.7	36.45	3.88	81.45	10.51	$\cdots$	3.1	7,8
F05563-3820	$\cdots$	0.32	0.65	13.48	$\cdots$	7.01	$\cdots$	122	$\cdots$	190	$\cdots$	6,10,19
MKN 6	1.25	9.74	5.45	30	24	76	7	216	$\cdots$	$\cdots$	22	1,25,20
MKN 9	5.4	0.65	2.6	26.65	3.3	10.05	$\cdots$	$\cdots$	$\cdots$	84.6	$\cdots$	1,3
MKN 79	3.22	7.89	4.04	68.5	10	35.1	$\cdots$	208.8	$\cdots$	261.7	$\cdots$	1,3,25
F07599+6508	$\cdots$	$\cdots$	$\cdots$	1.1	$\cdots$	0.33	$\cdots$	37	$\cdots$	$\cdots$	$\cdots$	1,21
NGC 2639	0.68	3.48	$\cdots$	0.7	1.09	2.34	1.17	2.96	10.71	$\cdots$	5.23	1,22
NGC 2782	$\cdots$	11.7	1.02	6.07	2.92	6.56	1.97	36.8	15.2	$\cdots$	15.6	1,8,22

Table 4—Continued

Name	[NeV][a]	[OII]	[NeIII]	Hβ	[OIII] 4959Å	[OIII] 5007Å	[OI]	Hα	[NII]	Hα + [NII]	[SII]	Ref
MKN 704	3.77	1.41	2.77	28.65	⋯	14.06	⋯	226.95	⋯	⋯	⋯	1,3,6,25
NGC 2841	⋯	⋯	⋯	0.59	⋯	1.09	0.33	1.94	3.57	⋯	2.2	22
UGC 5101	⋯	0.81	⋯	0.2	0.24	0.45	0.29	3.87	4.91	⋯	1.56	1,23,30
NGC 2992	⋯	11.4	2.46	2.7	9.13	29.3	3.11	19.7	16.55	⋯	11.66	1,7,25
MKN 1239	6.27	3.61	5.56	22.05	7.92	27.5	1.93	⋯	⋯	158.25	6	1,3,10
NGC 3031	1.09	5.43	5.27	19.8	8.2	22.6	23.5	113.8	41.8	⋯	25.8	26
MKN 1243	⋯	⋯	⋯	1.31	⋯	7.01	⋯	⋯	⋯	⋯	⋯	9
3C 234	0.85	1.41	⋯	2.12	⋯	15.7	0.21	⋯	⋯	⋯	⋯	1
NGC 3227	1.8	14	3.2	22.8	19	61.8	10.8	144.4	62.2	167.6	31.8	1,3,22
NGC 3511	⋯	⋯	⋯	1.43	⋯	0.72	⋯	7.02	2.53	⋯	3.51	27
NGC 3516	4.2	2.4	3.5	87.33	14	36.31	⋯	264.45	16.4	324.85	⋯	1,3,8,18,22
MKN 744	⋯	⋯	⋯	⋯	⋯	⋯	⋯	⋯	⋯	⋯	⋯	
NGC 4051	7.7	21	7.1	24.8	14	39.45	⋯	80.4	20.7	140	11.3	1,3,22
UGC 7064	1.22	2.48	1.41	1.11	4.49	11.54	0.97	4.31	4.53	⋯	1.24	1
NGC 4151	96	210	110	502.9	1000	1264.1	⋯	1384.7	220	2064.5	⋯	1,3,18
NGC 4235	⋯	⋯	⋯	3.13	⋯	2.01	1.02	28.7	3.09	⋯	2.33	3,17,22
NGC 4253	3.7	3.82	3.46	16.8	11.8	51.75	1.32	92.8	⋯	87.6	3.52	1,3
MKN 205	1.2	0.55	0.96	25.9	1.1	3.8	⋯	⋯	⋯	74	⋯	1
NGC 4395	⋯	⋯	⋯	2.3	⋯	14.4	1.91	9.85	2.16	⋯	4.7	17,22
3C 273	⋯	⋯	⋯	15.9	⋯	⋯	⋯	⋯	⋯	⋯	⋯	1
NGC 4565	⋯	⋯	⋯	0.17	⋯	1.46	0.26	0.77	2.08	⋯	0.81	17,22
NGC 4579	0.84	18.35	1.55	2.52	3.42	7.24	4.27	8.53	17.7	⋯	14.42	1,14,17,22
NGC 4593	⋯	⋯	⋯	50.9	7.1	16.3	⋯	297	⋯	128	⋯	1,3
NGC 4594	⋯	2.11	⋯	⋯	3.71	8.93	⋯	15.66	18.9	⋯	8.08	1,6
NGC 4602	⋯	⋯	⋯	⋯	⋯	⋯	⋯	⋯	⋯	⋯	⋯	
M-2-33-34	1.88	5.47	1.88	11.68	9.11	29.97	1.17	⋯	⋯	58.6	7.37	1,7,14
MKN 231	⋯	⋯	⋯	45	5.5	16.5	⋯	⋯	5	293	⋯	18
NGC 5033	0.61	2.75	⋯	1.1	⋯	5.26	1.61	10.13	11.79	⋯	4.42	1,17,22

Table 4—Continued

Name	[NeV][a]	[OII]	[NeIII]	Hβ	[OIII] 4959Å	[OIII] 5007Å	[OI]	Hα	[NII]	Hα + [NII]	[SII]	Ref
M-6-30-15	···	1.8	0.8	9.2	3.5	10.7	···	68.1	···	71.5	2.55	1,7,10
F13349+2438	0.11	0.73	···	17.2	···	6.88	···	246.3	···	114.8	···	1,16
IRAS 13354+3924	···	···	···	···	···	···	···	···	···	···	···	
NGC 5252	···	···	···	0.9	2.26	6.81	1.77	5.73	4.22	···	3.97	2,13
NGC 5273	···	···	···	1.18	4.1	12.05	1.13	5.05	5.23	···	3.65	2,22
IC 4329A	···	1.11	1.11	39.9	9.94	25.5	3.32	469.6	···	372	9.14	1,7,10
MKN 279	2.2	7.9	5.6	49.27	4.3	11.51	···	151.95	23.92	181	···	1,3,8
NGC 5548	7.18	6.52	8.63	59.45	15.33	46.77	1.9	···	···	269.2	3.76	1
MKN 471	0.4	0.73	0.61	···	···	···	···	13.3	···	···	···	1
NGC 5674	···	···	···	···	···	···	···	···	···	···	···	
MKN 817	···	···	···	33.95	···	12.49	···	138.1	1.69	···	···	3,8
MKN 841	2.37	3.31	2.11	25.9	8.81	26.2	0.08	···	···	115	3.33	1
F15091-2107	···	3.14	0.95	15	7.39	19.1	···	129.32	11.41	···	8.06	7,8
NGC 5905	···	···	···	1.71	···	0.44	0.11	7.41	2.97	···	1.57	22
CGCG 022-021	···	···	···	···	···	···	···	···	···	···	···	
IRAS 16146+3549	···	···	···	···	···	···	···	···	···	···	···	
E141-G55	6.85	···	···	79.13	7.64	20.95	···	381.88	35.32	···	7.64	3,7,8
NGC 6860	···	4.75	···	14.2	3.5	6.02	1.7	77.05	7.02	···	3.04	7,8
MKN 509	7.4	14.25	14	134.57	20.7	70.73	3.02	248.9	···	547.8	9.42	1,3
NGC 7213	···	21.35	7.88	22.85	20.2	23.85	28.5	180.5	24.66	···	19.9	7,8
E344-G16	···	0.89	···	4.56	1.3	2.61	···	44.83	···	···	···	6,7,8
3C 445	···	1.54	···	8.69	···	25.15	1.29	67.3	···	85.2	2.47	1,6
NGC 7314	···	0.17	0.1	3.77	0.85	4.79	0.24	18	1.5	···	0.85	3,7
UGC 12138	···	···	···	4.84	4.8	13.66	0.6	28.19	8.42	···	1.35	2,8
NGC 7469	9.2	18	9.7	102.45	14.63	45.38	···	···	14	427.5	···	1,18
NGC 7603	2.2	3.1	1.9	7.87	2.3	4.8	···	···	···	41.1	···	1,3
Seyfert 2												
NGC 34	0.07	3.2	···	0.32	0.35	0.91	0.75	6.53	7.82	···	3.39	1,23,30

Table 4—Continued

Name	[NeV][a]	[OII]	[NeIII]	Hβ	[OIII] 4959Å	[OIII] 5007Å	[OI]	Hα	[NII]	Hα + [NII]	[SII]	Ref
F00198-7926	⋯	⋯	⋯	0.32	⋯	2.38	⋯	1.55	0.73	⋯	⋯	4,8
NGC 262	0.76	12.79	4.76	5.63	20.4	51.68	4.64	17.82	17	17.2	⋯	1,3,6,18,25,28
F00521-7054	⋯	⋯	⋯	0.71	1.69	7.02	0.46	5.47	3.44	⋯	1.17	6,8,13,29
E541-IG12	⋯	⋯	⋯	0.32	⋯	2.12	⋯	1.38	0.99	⋯	⋯	6,8
NGC 424	⋯	5.42	4.14	9.12	⋯	41.7	⋯	⋯	⋯	⋯	⋯	3,25
NGC 513	⋯	4.8	1.51	1.61	1.96	4.9	0.55	4.91	3.67	⋯	2.24	1,28
MKN 573	⋯	23.1	7.48	10.51	⋯	138.34	⋯	63.09	22.7	⋯	⋯	3,6,8,25
F01475-0740	⋯	⋯	⋯	1.02	⋯	5.35	⋯	7.66	4.23	⋯	⋯	1,6
NGC 833	⋯	⋯	⋯	⋯	⋯	⋯	⋯	⋯	⋯	⋯	⋯	
NGC 839	⋯	⋯	⋯	1.3	⋯	1.31	⋯	8.71	5.67	⋯	⋯	8
UGC 2024	⋯	⋯	⋯	0.69	⋯	14.45	⋯	11.43	⋯	⋯	⋯	6,8
NGC 1052	⋯	⋯	⋯	10.51	⋯	21.05	27.6	30.15	33.65	⋯	66.9	8,22
NGC 1068	171.6	194.8	181.98	178.48	680	1629.8	56.6	773.75	1450.5	1861	277.3	1,3,14,18,29,25
NGC 1125	⋯	2.71	0.83	1.67	5.5	15.65	2.16	⋯	⋯	31.2	8.06	1
NGC 1143/4	⋯	0.83	⋯	0.37	1.55	4.65	0.3	2.41	3.49	⋯	1.53	1,4,21
M-2-8-39	1.6	1.36	1.15	0.95	5.77	17.25	1.2	6.56	3.49	⋯	1.77	1,6
NGC 1194	⋯	0.19	0.26	⋯	1.02	10.7	0.12	5.43	1	⋯	1.2	1,6
NGC 1241	⋯	0.38	⋯	0.41	1.06	1.56	0.51	3.2	3.49	⋯	1.97	1
NGC 1320	4.35	1.47	0.88	1.18	4.32	12.38	0.77	6.54	4.66	⋯	2.78	1,3,6
NGC 1386	⋯	51.9	18.47	5.25	⋯	293.2	⋯	94.85	⋯	⋯	⋯	3,6,25
F03362-1642	0.19	0.66	⋯	0.34	1.06	2.59	0.26	2.25	1.65	⋯	1.31	1,8
NGC 1433	⋯	⋯	⋯	⋯	⋯	⋯	⋯	9.7	14.9	⋯	9.49	14
E420-G13	⋯	⋯	⋯	⋯	⋯	25.5	⋯	16.1	⋯	⋯	⋯	6
IRAS 04259-0440	⋯	⋯	⋯	0.18	⋯	0.34	0.17	1.4	1.04	⋯	0.77	21
NGC 1614	⋯	11	⋯	8.66	⋯	9.12	2.36	96.2	54.75	⋯	21.4	14,21
NGC 1667	0.61	3.31	0.43	1.04	2.42	6.03	1.38	10.66	10.5	⋯	5.55	1,3,14,25
NGC 1672	⋯	16.9	⋯	25.3	⋯	9.98	⋯	170.7	80.5	⋯	41	14
E33-G2	⋯	⋯	⋯	0.75	⋯	6.77	⋯	5.64	4.49	⋯	⋯	6,8

Table 4—Continued

Name	[NeV][a]	[OII]	[NeIII]	Hβ	[OIII] 4959Å	[OIII] 5007Å	[OI]	Hα	[NII]	Hα + [NII]	[SII]	Ref
NGC 1808	···	···	···	5.75	···	1.45	···	81.5	···	···	···	29
F05189-2524	···	···	···	0.22	2.07	7.99	0.38	3.14	5.29	···	0.99	13,21,23,30
NGC 2655	···	···	···	···	···	3.91	5.2	5.01	14.6	···	9.62	22
NGC 2683	···	···	···	0.1	···	0.3	0.14	0.42	0.62	···	0.58	22
F08572+3915	0.17	0.63	···	0.06	···	0.16	0.09	0.7	0.29	···	0.45	1,30,31
NGC 3079	···	···	···	0.05	···	0.18	0.21	1.18	1.87	···	1.01	22
NGC 3147	···	···	···	0.28	···	1.72	0.22	1.48	4.01	···	1.69	22
NGC 3362	···	···	···	0.75	2.25	6.78	0.63	2.77	5.92	···	2.15	2,29
NGC 3486	···	···	···	0.29	···	1.31	0.09	0.96	1	···	0.89	22
UGC 6100	···	···	···	···	···	···	···	···	···	···	···	
NGC 3593	···	···	···	0.66	···	0.93	0.16	3.89	2.14	···	1.44	22
NGC 3627	···	···	···	1.02	···	2.95	0.78	6.02	8.67	···	4.46	22
M 0-29-23	···	0.79	0.23	0.52	0.5	0.78	0.38	7.64	4.94	···	1.8	1,23,30
NGC 3660	···	···	···	0.37	1.6	2.94	···	5.59	4.57	10	0.9	1,14
NGC 3735	···	···	···	0.53	···	3.74	0.18	3.31	2.81	···	1.26	22
NGC 3822	···	···	···	···	···	···	···	···	···	···	···	
NGC 3976	···	···	···	0.22	···	0.77	0.1	0.96	1.87	···	0.8	22
NGC 3982	1.6	2.81	3.29	1.25	5.78	18.1	1.79	4.3	4.24	···	2.77	1,22
NGC 4303	···	···	···	3.61	···	4.91	0.65	14.5	11.3	···	5.78	22
NGC 4388	···	13.47	3.62	4.06	19.3	48.87	136	19.47	8.38	···	5.27	3,4,8,28,25
IC 3639	3.94	21	3.91	6.45	14.5	37.35	4.9	32.97	24.35	79.6	22.7	1,6,8,14
NGC 4628	···	···	···	···	···	···	···	···	···	···	···	
NGC 4826	···	···	···	1.3	···	1.96	0.53	7.24	9.2	···	5.56	22
NGC 4922	0.26	2.41	···	1.22	1.36	3.47	0.62	8.1	5.41	···	2.54	1,6,30
NGC 4941	···	7.05	1.73	2	12.3	27.45	3	9.49	21.3	···	9.8	1,6,25
NGC 4968	···	···	···	0.64	6.9	13.43	1.32	6.17	7.1	29	3.72	1,2,3
NGC 5005	0.76	15.9	1.54	···	···	9.79	0.83	6.4	7.1	···	2.84	1
M-3-34-64	···	···	···	13.06	···	153	9.82	44.02	56.61	···	20.03	2,4,13

Table 4—Continued

Name	[NeV][a]	[OII]	[NeIII]	Hβ	[OIII] 4959Å	[OIII] 5007Å	[OI]	Hα	[NII]	Hα + [NII]	[SII]	Ref
NGC 5135	2.48	4.15	1.64	6.89	12.6	32	3.7	47.74	60	122	21.55	1,3,14,25
NGC 5194	⋯	⋯	⋯	1.29	⋯	16.3	1.71	11.45	31.1	⋯	10.2	6,22
NGC 5248	⋯	⋯	⋯	0.59	⋯	0.17	0.15	4.17	2.17	⋯	1	22
NGC 5256	1.75	4.79	0.86	1.22	0.52	3.22	0.69	5.15	3.93	⋯	2.81	3,4,6,23,21,25
MKN 270	0.64	17	4.01	2.19	11	28.95	⋯	8.31	⋯	34.3	⋯	1,3,25
NGC 5278	⋯	⋯	⋯	⋯	⋯	⋯	⋯	⋯	⋯	⋯	⋯	
MKN 273	0.41	9.4	1.6	3.06	5.39	17.96	3.67	28.2	29.3	48.7	17.5	1,3,23
MKN 796	⋯	25.2	2.23	9.91	6.51	12.06	1.36	48.9	19.35	⋯	10.54	1,30
MKN 1361	⋯	⋯	⋯	1.99	⋯	9.73	1.06	28	9.06	⋯	5.46	30
MKN 461	⋯	5.87	1.34	3.74	1.27	4.22	⋯	⋯	⋯	⋯	⋯	28
NGC 5347	1.02	1.46	0.86	0.36	2.11	5.38	0.81	3.19	2.72	⋯	1.95	1,6
MKN 463	1.6	21	5.65	9.12	30.57	75.69	-0.61	35.87	14.38	70	16	1,8,13,25
NGC 5395	⋯	⋯	⋯	0.06	⋯	0.18	0.49	0.29	0.35	⋯	0.22	22
NGC 5506	1.26	17.5	4.33	5.09	10.7	43.73	5.61	45.53	30.45	⋯	24.1	3,6,13,14,25
MKN 686	⋯	4.6	0.94	2.76	4.09	23.37	-1.94	11.14	13.39	⋯	8.45	28
NGC 5899	0.82	2.36	⋯	2.09	5.58	23.87	2.32	8.2	17.47	⋯	8.04	1,4
NGC 5929	⋯	9.85	1.15	2.34	3.96	9.83	3.24	12.85	8.14	⋯	9.92	1,3
NGC 5953	1.54	12.1	2.92	5.22	7.95	12.31	2.15	32.4	21.75	⋯	15.19	1,6,30
UGC 9913	⋯	⋯	⋯	1.4	⋯	0.43	0.28	1.42	2.73	⋯	1.28	6,30
UGC 9944	1.56	3.3	1.11	1.53	2.63	14.6	1.42	9.29	9.17	⋯	2.01	1
NGC 5995	⋯	⋯	⋯	0.34	⋯	2.16	0.06	1.06	1.09	⋯	0.24	4
F15480-0344	0.82	0.77	⋯	0.89	⋯	15.95	0.53	6.37	3.65	⋯	1.4	1,2,13
NGC 6217	⋯	⋯	⋯	9.66	⋯	2.6	1.19	37.2	23.8	⋯	10.8	22
NGC 6240	⋯	⋯	⋯	0.53	⋯	0.76	2.63	8.5	10.7	⋯	10.5	30
NGC 6552	⋯	⋯	⋯	⋯	⋯	⋯	⋯	⋯	⋯	⋯	⋯	
NGC 6810	⋯	⋯	⋯	1.08	⋯	0.65	⋯	13.7	8.52	⋯	4.13	27
E339-G11	⋯	⋯	⋯	⋯	⋯	⋯	⋯	⋯	⋯	⋯	⋯	
NGC 6890	⋯	2.04	1.89	0.89	⋯	19.1	⋯	3.72	⋯	⋯	⋯	3,25

Table 4—Continued

Name	[NeV][a]	[OII]	[NeIII]	Hβ	[OIII] 4959Å	[OIII] 5007Å	[OI]	Hα	[NII]	Hα + [NII]	[SII]	Ref
I5063	$\cdots$	16.69	4.57	7.6	$\cdots$	74.85	$\cdots$	43.2	21.1	$\cdots$	$\cdots$	3,8,25
MKN 897	$\cdots$	0.52	0.24	0.36	1.46	3.71	0.23	1.55	1.77	$\cdots$	0.31	1
NGC 7130	$\cdots$	13	4.6	5.39	$\cdots$	28.3	1.01	33.82	26.54	$\cdots$	8.37	4,14,25
NGC 7172	$\cdots$	$\cdots$	$\cdots$	0.08	$\cdots$	0.4	0.03	0.29	0.29	$\cdots$	0.13	4
F22017+0319	3.51	3.8	$\cdots$	2.67	5.99	24.33	0.8	9.81	4.31	$\cdots$	3.13	1,6,13
IC 5169	$\cdots$	$\cdots$	$\cdots$	$\cdots$	$\cdots$	1	$\cdots$	$\cdots$	$\cdots$	14.11	$\cdots$	3,32
M-3-58-07	$\cdots$	$\cdots$	$\cdots$	1.61	$\cdots$	12.74	$\cdots$	6.18	6.31	$\cdots$	$\cdots$	8
NGC 7479	$\cdots$	$\cdots$	$\cdots$	0.35	$\cdots$	1.4	0.38	1.72	2.06	$\cdots$	1.74	4,8,22
NGC 7496	$\cdots$	12.3	$\cdots$	7.2	1.08	4.89	117	42.95	21	$\cdots$	11.99	13,14
E148-IG2	$\cdots$	$\cdots$	$\cdots$	1.05	1.02	2.82	0.45	10.2	2.06	$\cdots$	2.21	13
IC 5298	$\cdots$	$\cdots$	$\cdots$	1.47	$\cdots$	6.03	0.31	6.37	6.51	$\cdots$	1.57	4,30
NGC 7582	2.1	13.8	6.2	15.17	23.3	45.3	4.43	105.65	72.7	134	32.6	3,14,28,25
NGC 7590	$\cdots$	8.04	$\cdots$	2.71	$\cdots$	5.52	$\cdots$	21.15	9.59	$\cdots$	7.96	6,14
NGC 7674	3.49	5.61	5.61	4.53	9.36	47.78	2.83	15.37	14.11	$\cdots$	8.12	1,3,4,13
NGC 7678	$\cdots$	0.88	$\cdots$	1	0.2	0.26	0.22	8.13	4.02	$\cdots$	2.03	24
NGC 7682	$\cdots$	8.86	2.57	2.5	8.3	24.17	2.6	9.57	10.6	$\cdots$	7.49	2,6,28
NGC 7733	$\cdots$	$\cdots$	$\cdots$	$\cdots$	$\cdots$	$\cdots$	$\cdots$	$\cdots$	$\cdots$	$\cdots$	$\cdots$	
CG381-051	$\cdots$	$\cdots$	$\cdots$	1.11	$\cdots$	0.51	$\cdots$	8.44	4.44	$\cdots$	$\cdots$	8
MKN 331	$\cdots$	$\cdots$	$\cdots$	2.16	$\cdots$	0.84	0.45	18	9.67	$\cdots$	4.84	30

[a]Emission line fluxes have units of 10^{-14} ergs cm^{-2} s^{-1}. The wavelengths for these lines can be found in Table 3.

References. — (1) Our data; (2) Osterbrock & Martel (1993); (3) Mulchaey et al. (1994); (4) Lumsden et al. (2001); (5) Moran et al. (1996); (6) Bonatto & Pastoriza (1997); (7) Winkler (1992); (8) de Grijp et al. (1992); (9) Ho & Peng (2001); (10) Morris & Ward (1989); (11) Poggianti & Wu (2000); (12) Coziol et al. (1993); (13) Young et al. (1996); (14) Storchi-Bergmann et al. (1995); (15) Sosa-Brito et al. (2001); (16) Boroson & Meyers (1992); (17) Ho et al. (1997b); (18) Lacy et al. (1982); (19) Rodríguez-Ardila et al. (2000); (20) Malkan & Oke (1983);

(21) Veilleux et al. (1999); (22) Ho et al. (1997a); (23) Kim et al. (1995); (24) Misselt et al. (1999); (25) Schmitt (1998); (26) Ho et al. (1996); (27) Kirhakos & Steiner (1990); (28) Cruz-Gonzalez et al. (1994); (29) Polletta et al. (1996); (30) Veilleux et al. (1995); (31) Armus et al. (1989); (32) Colbert et al. (1996) .

Table 5.   Ultraviolet Data

Name	Lyman α[a]	Ly α EW[b]	N V	N V EW	CIV	CIV EW	CIII]	CIII] EW	MgII	MgII EW	F_{UV}[c]	λ (Å)	Ref
Seyfert 1													
MKN 335	828	109.3	280	36.45	347.48	78.97	125.9	23.17	55.79	67.55	7.89	1417.5	1,6,9,19
E12-G21	22	$\cdots$	14	$\cdots$	12	$\cdots$	3.1	$\cdots$	13	$\cdots$	0.29	1450	2
I ZW 1	143.05	136.5	$\cdots$	$\cdots$	44.27	24.67	70	25.39	89.83	49.4	2.35	1483.3	3,6,7,9
NGC 1097	$\cdots$	$\cdots$	$\cdots$	$\cdots$	$\cdots$	$\cdots$	$\cdots$	$\cdots$	$\cdots$	$\cdots$	2.11	1507	4
F03450+0055	17.7	101	$\cdots$	$\cdots$	7.8	73	2.13	29.3	$\cdots$	$\cdots$	0.11	1500	6
NGC 1566	23.1	101	3.65	8	28.6	92	10.95	35.5	26.26	168.5	0.23	1475	2,7
3C 120	78.9	79	$\cdots$	$\cdots$	36.4	131	$\cdots$	$\cdots$	$\cdots$	$\cdots$	0.74	1335	1,9
MKN 6	$\cdots$	$\cdots$	$\cdots$	$\cdots$	46	200	40	200	73	100	$\cdots$	$\cdots$	8
MKN 9	254	$\cdots$	$\cdots$	$\cdots$	38	78	$\cdots$	$\cdots$	$\cdots$	$\cdots$	1.86	1335	1
MKN 79	100.95	126	18.7	21.9	75.45	96.5	8	10	30	29	$\cdots$	$\cdots$	9,10
MKN 704	14.6	91	$\cdots$	$\cdots$	11.7	76	$\cdots$	$\cdots$	$\cdots$	$\cdots$	0.8	1335	1,9
NGC 2841	52.1	50.2	11.7	11.7	21.85	29.5	7.14	13	$\cdots$	$\cdots$	0.49	1500	7
NGC 3031	146.5	707.5	6.55	54	23.37	159.2	23.19	158.4	56.87	397.3	0.28	1502.3	6,7,11
3C 234	$\cdots$	$\cdots$	$\cdots$	$\cdots$	6.26	145.5	1.35	39.7	$\cdots$	$\cdots$	$\cdots$	$\cdots$	17
NGC 3516	$\cdots$	$\cdots$	$\cdots$	$\cdots$	17	148	$\cdots$	$\cdots$	$\cdots$	$\cdots$	1.63	1335	1,6
MKN 744	$\cdots$	$\cdots$	$\cdots$	$\cdots$	$\cdots$	$\cdots$	$\cdots$	$\cdots$	$\cdots$	$\cdots$	0.15	1500	6
NGC 4051	$\cdots$	$\cdots$	$\cdots$	$\cdots$	11	72	$\cdots$	$\cdots$	$\cdots$	$\cdots$	1.01	1335	1
UGC 7064	$\cdots$	$\cdots$	$\cdots$	$\cdots$	$\cdots$	$\cdots$	$\cdots$	$\cdots$	$\cdots$	$\cdots$	0.07	1500	6
NGC 4151	6110	113.47	26.7	0.63	7215	167.2	$\cdots$	$\cdots$	1007	59.65	45.69	1500	6,7
MKN 205	229.33	116.15	7.3	2.4	95.97	97.1	30.09	13.47	60	48.22	1.58	1428.3	1,3,7
NGC 4395	$\cdots$	$\cdots$	$\cdots$	$\cdots$	50.42	364.7	8.3	60.5	5.39	39.9	0.14	1500	7
3C 273	959.25	55.73	$\cdots$	$\cdots$	221.95	27.73	519	28.94	211.2	22.94	19.25	1428.3	1,3,7,9
NGC 4579	33.8	990	1.8	55	10.5	362	7.49	252.6	8.95	369.8	0.16	1503.5	4,6
NGC 4593	$\cdots$	$\cdots$	$\cdots$	$\cdots$	19	112.5	$\cdots$	$\cdots$	$\cdots$	$\cdots$	1.19	1335	1,9
NGC 4594	$\cdots$	$\cdots$	$\cdots$	$\cdots$	$\cdots$	$\cdots$	$\cdots$	$\cdots$	$\cdots$	$\cdots$	0.34	1507	4,6
M-2-33-34	43.12	$\cdots$	$\cdots$	$\cdots$	24.28	$\cdots$	11.28	$\cdots$	10.4	$\cdots$	1.03	1507	4
MKN 231	6.3	33.3	0.9	5	1.7	10.1	0.7	3.8	$\cdots$	$\cdots$	0.16	1500	6

60 —

Table 5—Continued

Name	Lyman α[a]	Ly α EW[b]	N V	N V EW	CIV	CIV EW	CIII]	CIII] EW	MgII	MgII EW	F_{UV}[c]	λ (Å)	Ref
M-6-30-15	$\cdots$	$\cdots$	$\cdots$	$\cdots$	25	140	$\cdots$	$\cdots$	$\cdots$	$\cdots$	$\cdots$	$\cdots$	18
F13349+2438	$\cdots$	$\cdots$	$\cdots$	$\cdots$	6.8	36.6	5.07	21.2	7.89	37.12	0.12	1500	6
NGC 5252	$\cdots$	$\cdots$	$\cdots$	$\cdots$	0.94	231	1.65	460	2.02	650	0	1500	6
MKN 279	108.4	91.5	4	2.2	101.2	96	14.4	11	$\cdots$	$\cdots$	$\cdots$	$\cdots$	9,10
NGC 5548	608.85	167.2	28	17.9	223.68	172.6	47.8	51.55	102.8	108.55	4.05	1417.5	1,7,9,10
MKN 817	$\cdots$	$\cdots$	$\cdots$	$\cdots$	320	120	75	29	120	63	$\cdots$	$\cdots$	19
MKN 841	63	85	$\cdots$	$\cdots$	34.8	48	$\cdots$	$\cdots$	$\cdots$	$\cdots$	$\cdots$	$\cdots$	9
E141-G55	545	87	$\cdots$	$\cdots$	82.75	81.5	$\cdots$	$\cdots$	$\cdots$	$\cdots$	7.97	1335	1,9
MKN 509	1132.67	138.35	180	12.8	522.9	120.39	267.1	30.91	280.7	50.47	8.37	1417.5	1,7,9
NGC 7213	$\cdots$	$\cdots$	$\cdots$	$\cdots$	13	143	$\cdots$	$\cdots$	$\cdots$	$\cdots$	1.08	1335	1
NGC 7469	371	96.1	206	31.7	269.73	99.87	126.8	28.7	211.9	67.4	5.03	1417.5	1,6,9
NGC 7603	33.2	177	6	$\cdots$	25.73	173	27	$\cdots$	52	$\cdots$	0.46	1392.5	1,2,9
Seyfert 2													
NGC 262	40.61	$\cdots$	$\cdots$	$\cdots$	9.86	$\cdots$	2.94	$\cdots$	1.66	110	$\cdots$	$\cdots$	6,11
MKN 573	$\cdots$	$\cdots$	$\cdots$	$\cdots$	$\cdots$	$\cdots$	$\cdots$	$\cdots$	0.7	50	$\cdots$	$\cdots$	6
NGC 1052	26.7	1070	0.11	5	0.54	19	1.08	51.3	2.42	132.5	$\cdots$	$\cdots$	6
NGC 1068	465	51.4	86	26.7	349.3	58.7	141.47	32.5	60.87	31.2	4.83	1504.6	4,7,11,14
NGC 1433	$\cdots$	$\cdots$	$\cdots$	$\cdots$	$\cdots$	$\cdots$	$\cdots$	$\cdots$	$\cdots$	$\cdots$	0.6	1507	4
NGC 1614	$\cdots$	$\cdots$	$\cdots$	$\cdots$	$\cdots$	$\cdots$	1.91	$\cdots$	$\cdots$	$\cdots$	0.5	1507	4,11
NGC 1667	7	16	$\cdots$	$\cdots$	$\cdots$	$\cdots$	$\cdots$	$\cdots$	$\cdots$	$\cdots$	0.18	1507	4,12
NGC 1672	$\cdots$	$\cdots$	$\cdots$	$\cdots$	$\cdots$	$\cdots$	$\cdots$	$\cdots$	$\cdots$	$\cdots$	2.97	1507	4
F05189-2524	5.27	$\cdots$	2.05	$\cdots$	2.85	$\cdots$	$\cdots$	$\cdots$	$\cdots$	$\cdots$	$\cdots$	$\cdots$	13
NGC 4388	12	$\cdots$	$\cdots$	$\cdots$	8	$\cdots$	1.7	$\cdots$	2.2	$\cdots$	$\cdots$	$\cdots$	14
IC 3639	$\cdots$	$\cdots$	$\cdots$	$\cdots$	$\cdots$	$\cdots$	$\cdots$	$\cdots$	1.22	13.9	1.19	1507	4,6
M-3-34-64	56	120	5	12	14	45	7	40	$\cdots$	$\cdots$	0.19	1600	15
NGC 5135	54.98	58	1.1	1	6.09	4	$\cdots$	$\cdots$	$\cdots$	$\cdots$	0.92	1507	4,12
MKN 270	20	$\cdots$	$\cdots$	$\cdots$	7.7	$\cdots$	4	$\cdots$	0.38	35.5	$\cdots$	$\cdots$	6,14
NGC 5506	$\cdots$	$\cdots$	$\cdots$	$\cdots$	$\cdots$	$\cdots$	5.93	$\cdots$	$\cdots$	$\cdots$	0.26	1507	4

Table 5—Continued

Name	Lyman α[a]	Ly α EW[b]	N V	N V EW	CIV	CIV EW	CIII]	CIII] EW	MgII	MgII EW	F_{UV}[c]	λ (Å)	Ref
NGC 5929	$\cdots$	$\cdots$	$\cdots$	$\cdots$	$\cdots$	$\cdots$	1.41	235	$\cdots$	$\cdots$	$\cdots$	$\cdots$	6
NGC 6217	$\cdots$	$\cdots$	$\cdots$	$\cdots$	$\cdots$	$\cdots$	$\cdots$	$\cdots$	$\cdots$	$\cdots$	1.69	1507	11
NGC 7130	18.4	31	2.6	5	1.6	4	$\cdots$	$\cdots$	$\cdots$	$\cdots$	0.74	1507	4,12
NGC 7496	$\cdots$	$\cdots$	$\cdots$	$\cdots$	$\cdots$	$\cdots$	$\cdots$	$\cdots$	$\cdots$	$\cdots$	1.55	1507	4
NGC 7582	$\cdots$	$\cdots$	$\cdots$	$\cdots$	0.72	7	0.35	2.4	0.31	1	0.16	1507	4,5
NGC 7590	$\cdots$	$\cdots$	$\cdots$	$\cdots$	$\cdots$	$\cdots$	$\cdots$	$\cdots$	$\cdots$	$\cdots$	0.34	1507	4
NGC 7674	46.98	$\cdots$	$\cdots$	$\cdots$	11.45	$\cdots$	7.94	$\cdots$	11.39	$\cdots$	$\cdots$	$\cdots$	16

[a]Emission line fluxes have units of 10^{-14} ergs cm^{-2} s^{-1}. The wavelengths for these lines can be found in Table 3.

[b]Equivalent widths are in Å.

[c]UV continuum flux is in units of 10^{-14} ergs cm^{-2} s^{-1} Å^{-1}.

References. — (1) Wang et al. (1996); (2) Clavel & Joly (1984); (3) Buson & Ulrich (1990); (4) Storchi-Bergmann et al. (1995); (5) Clavel et al. (1980); (6) Kuraszkiewicz et al. (2004); (7) Kuraszkiewicz et al. (2002); (8) Malkan & Oke (1983); (9) Wang et al. (1998); (10) Barr et al. (1983); (11) McQuade et al. (1995); (12) Thuan (1984); (13) Farrah et al. (2005); (14) Ferland & Osterbrock (1986); (15) De Robertis et al. (1988); (16) Kraemer et al. (1994); (17) Kishimoto et al. (2001); (18) Reynolds et al. (1997); (19) Grandi (1983) .

Table 6.   Luminosity Function Parameters

Line	Type	Log $\Phi_\star$	Log $L_\star$
Hα	Sy 1	-4.18 ± 0.34	41.04 ± 0.13
	Sy 2	-3.77 ± 0.30	39.92 ± 0.12
Hβ	Sy 1	-4.37 ± 0.31	40.72 ± 0.14
	Sy 2	-3.93 ± 0.30	39.24 ± 0.12
[N II]	Sy 1	-4.10 ± 0.46	39.98 ± 0.18
	Sy 2	-3.76 ± 0.31	39.79 ± 0.12
[O I]	Sy 1	-4.50 ± 0.52	39.38 ± 0.20
	Sy 2	-4.21 ± 0.28	39.36 ± 0.13
[O II]	Sy 1	-4.13 ± 0.39	39.58 ± 0.16
	Sy 2	-4.27 ± 0.44	39.78 ± 0.17
[O III] $\lambda4969$	Sy 1	-4.26 ± 0.37	39.96 ± 0.16
	Sy 2	-4.38 ± 0.49	39.75 ± 0.18
[O III] $\lambda5007$	Sy 1	-4.11 ± 0.38	40.25 ± 0.15
	Sy 2	-3.99 ± 0.25	40.09 ± 0.11
[S II]	Sy 1	-3.98 ± 0.45	39.59 ± 0.18
	Sy 2	-3.78 ± 0.31	39.56 ± 0.13

Note. — Best fit parameters of $\Phi_\star$ and $L_\star$ for our luminosity functions, described in Section 2. The assumed luminosity function is a double power law with breaks at L_* is given by Equation 1. $\Phi_\star$ has units of Mpc^{-3} mag^{-1} and $L_\star$ has units of ergs s^{-1}.

Table 7.   Ionization Averages

Log(Line-Ratio)	Sy Type	Average
[Ne III]*/[O II]	1, 1.2, 1.5	-0.11 ± 0.38
	1.8, 1.9	-0.33 ± 0.31
	2	-0.48 ± 0.30
[O III]/[O II]	1, 1.2, 1.5	0.71 ± 0.48
	1.8, 1.9	0.38 ± 0.49
	2	0.43 ± 0.52
[Ne V]/[Ne III]	1, 1.2, 1.5	-0.03 ± 0.22
	1.8, 1.9	-0.29 ± 0.27
	2	-0.17 ± 0.40

Note. — This is a list of the line ratio averages divided by type. The Seyfert 1, 1.2, and 1.5's have higher ratios than Seyfert 1.8, 1.9, and 2's.

*Although the Seyfert 1s appear to have slightly stronger [Ne III]$\lambda3869$ emission, relative to [O III], as discussed in the text we attribute this to unremoved contamination from the BLR emission of He I$\lambda3889$, rather than an intrinsic NLR difference between Sy 1 and Sy 2 galaxies.

Table 8.   Fits and Errors for Reddening Ratios

Ratios	Type	A	B
Hα/Hβ vs. [S II]/[O II]	Sy 1	0.44 ± 0.14	0.69 ± 0.03
Hα/Hβ vs. [S II]/[O II]	Sy 2	0.44 ± 0.22	0.73 ± 0.04
Hα/Hβ vs. [N II]/[O II]	Sy 1	0.25 ± 0.13	0.61 ± 0.04
Hα/Hβ vs. [N II]/[O II]	Sy 2	0.17 ± 0.13	0.71 ± 0.05
Hα/Hβ vs. [O III]/[Ne III]	Sy 1	0.33 ± 0.12	0.39 ± 0.10
Hα/Hβ vs. [O III]/[Ne III]	Sy 2	0.20 ± 0.54	0.56 ± 0.53
[S II]/[O II] vs. [O III]/[Ne III]	Sy 1	1.65 ± 0.47	-1.40 ± 0.43
[S II]/[O II] vs. [O III]/[Ne III]	Sy 2	2.56 ± 1.26	-2.40 ± 1.22
[O III]/[Ne III] vs. [N II]/[O II]	Sy 2	0.59 ± 0.50	0.66 ± 0.17
[O III]/[Ne III] vs. [N II]/[O II]	Sy 2	0.27 ± 0.18	0.88 ± 0.07
[S II]/[O II] vs. [N II]/[O II]	Sy 1	0.87 ± 0.10	-0.22 ± 0.05
[S II]/[O II] vs. [N II]/[O II]	Sy 2	0.83 ± 0.10	-0.18 ± 0.05

Note. — A and B are the slope and intercept from the Least Squares Orthogonal Fit, respectively.

Table 9.   IR, NUV, and HX Luminosities for Seyfert Galaxies

Seyfert 1	IR 10 μm	IR 2 μm	NUV 2267Å	HX 2-10 keV	Seyfert 2	IR 10 μm	IR 2 μm	NUV 2267Å	HX 2-10 keV
MKN 334	43.81	$\cdots$	43.01	$\cdots$	NGC 34	$\cdots$	42.75	$\cdots$	$\cdots$
MKN 355	$\cdots$	43.46	43.81	43.40	IRAS F00198-7926	$\cdots$	43.49	44.58	42.32
E 540-G1	$\cdots$	42.35	45.92	$\cdots$	M-4-2-18	$\cdots$	$\cdots$	43.91	$\cdots$
E12-G21	$\cdots$	43.09	$\cdots$	$\cdots$	NGC 262	42.92	42.37	43.65	43.45
UGC 00524	$\cdots$	$\cdots$	$\cdots$	$\cdots$	IRAS F00521-7054	$\cdots$	43.97	44.52	$\cdots$
IZW1	45.78	44.27	44.02	43.80	E541-IG12	$\cdots$	43.77	44.22	$\cdots$
MKN 993	$\cdots$	$\cdots$	43.47	42.91	NGC 424	$\cdots$	42.96	43.04	42.47
UGC 01395	$\cdots$	42.94	42.99	$\cdots$	NGC 513	43.31	42.19	44.52	42.64
MKN 590	$\cdots$	$\cdots$	$\cdots$	$\cdots$	MKN 573	$\cdots$	$\cdots$	43.87	$\cdots$
NGC 526A	$\cdots$	$\cdots$	43.13	$\cdots$	IRAS F01475-0740	$\cdots$	41.74	$\cdots$	41.75
MKN 1034	44.27	$\cdots$	43.45	$\cdots$	NGC 833	$\cdots$	$\cdots$	42.58	$\cdots$
M-3-7-11	$\cdots$	42.67	43.73	$\cdots$	NGC 839	$\cdots$	42.34	43.54	$\cdots$
NGC 931	43.39	42.73	$\cdots$	42.54	UGC 2024	$\cdots$	41.41	43.42	$\cdots$
NGC 1365	$\cdots$	42.51	41.89	41.24	NGC 1052	$\cdots$	39.63	41.94	$\cdots$
IRAS F03450+0055	44.11	43.41	43.25	$\cdots$	NGC 1056	$\cdots$	$\cdots$	42.88	$\cdots$
NGC 1566	$\cdots$	41.49	$\cdots$	$\cdots$	NGC 1068	42.89	$\cdots$	$\cdots$	43.11
3C 120	44.25	43.58	$\cdots$	43.95	NGC 1097	$\cdots$	$\cdots$	41.47	40.51
MKN 618	44.12	43.50	$\cdots$	43.40	NGC 1125	$\cdots$	$\cdots$	$\cdots$	$\cdots$
M-5-13-17	42.72	41.93	43.17	$\cdots$	NGC 1143	$\cdots$	40.44	42.31	43.47
IRAS F05563-3820	$\cdots$	43.83	44.13	43.92	M-2-8-39	$\cdots$	41.85	42.39	42.77
MKN 6	$\cdots$	43.24	43.19	43.11	NGC 1194	$\cdots$	$\cdots$	43.41	42.62
MKN 9	44.33	43.59	44.08	$\cdots$	NGC 1241	42.67	39.92	42.66	$\cdots$
MKN 79	43.89	43.16	43.45	43.33	NGC 1320	42.32	41.82	42.60	43.10
IRAS F07599+6508	$\cdots$	$\cdots$	$\cdots$	42.12	NGC 1386	$\cdots$	39.95	42.07	40.75
NGC 2639	$\cdots$	39.88	42.26	40.34	IRAS F03362-1642	$\cdots$	$\cdots$	$\cdots$	$\cdots$
NGC 2782	$\cdots$	41.39	42.02	$\cdots$	NGC 1433	$\cdots$	$\cdots$	43.99	$\cdots$
MKN 704	$\cdots$	43.36	43.70	43.31	E420-G13	$\cdots$	42.04	42.91	$\cdots$

Table 9—Continued

Seyfert 1	*IR* 10 μm	*IR* 2 μm	*NUV* 2267Å	*HX* 2-10 keV	Seyfert 2	*IR* 10 μm	*IR* 2 μm	*NUV* 2267Å	*HX* 2-10 keV
NGC 2841	$\cdots$	38.96	41.08	$\cdots$	IRAS F04259-0440	$\cdots$	41.30	$\cdots$	$\cdots$
UCG 5101	44.35	43.42	43.67	42.45	NGC 1614	$\cdots$	42.57	$\cdots$	$\cdots$
NGC 2992	41.90	41.85	42.71	43.07	IRAS F04385-0828	$\cdots$	42.51	$\cdots$	$\cdots$
MKN 1239	43.81	43.48	$\cdots$	$\cdots$	NGC 1672	$\cdots$	$\cdots$	$\cdots$	41.15
NGC 3031	36.13	$\cdots$	38.15	38.36	NGC 1667	$\cdots$	40.79	41.76	$\cdots$
MKN 1243	$\cdots$	$\cdots$	$\cdots$	$\cdots$	E33-G2	$\cdots$	42.56	$\cdots$	$\cdots$
3c234	47.26	44.20	45.50	44.34	NGC 1808	$\cdots$	$\cdots$	41.38	$\cdots$
NGC 3227	40.82	41.69	42.27	41.67	IRAS F05189-2524	44.83	43.85	43.86	43.25
NGC 3511	40.42	38.31	41.86	$\cdots$	E253-G3	$\cdots$	43.18	44.42	$\cdots$
NGC 3516	$\cdots$	42.38	$\cdots$	42.54	NGC 2655	$\cdots$	39.26	42.47	$\cdots$
MKN 744	$\cdots$	$\cdots$	$\cdots$	$\cdots$	NGC 2683	$\cdots$	41.12	40.75	38.21
NGC 4051	40.23	41.41	41.83	41.29	IRAS F08572+3915	$\cdots$	42.94	$\cdots$	42.06
UCG 7064	$\cdots$	42.46	43.20	$\cdots$	NGC 3079	40.28	41.84	41.34	41.09
NGC 4151	41.41	39.79	$\cdots$	42.11	NGC 3094	42.55	$\cdots$	$\cdots$	$\cdots$
NGC 4235	$\cdots$	39.47	42.28	42.22	NGC 3147	$\cdots$	40.30	42.43	$\cdots$
NGC 4253	42.99	39.67	42.86	42.89	NGC 3362	$\cdots$	$\cdots$	43.06	$\cdots$
MKN 205	$\cdots$	$\cdots$	44.67	$\cdots$	NGC 3486	$\cdots$	38.34	41.31	$\cdots$
NGC 4395	$\cdots$	$\cdots$	40.11	39.81	UGC6100	$\cdots$	$\cdots$	43.29	$\cdots$
3c273	$\cdots$	$\cdots$	46.11	$\cdots$	NGC 3593	$\cdots$	40.50	41.40	$\cdots$
NGC 4565	$\cdots$	$\cdots$	41.82	$\cdots$	NGC 3627	$\cdots$	40.62	41.73	37.88
NGC 4579	$\cdots$	$\cdots$	41.68	41.28	M 0-29-23	$\cdots$	42.52	$\cdots$	$\cdots$
NGC 4593	42.36	42.50	41.59	42.80	NGC 3660	$\cdots$	41.04	42.80	41.84
NGC 4594	39.76	39.76	$\cdots$	$\cdots$	NGC 3735	$\cdots$	$\cdots$	42.65	$\cdots$
NGC 4602	$\cdots$	$\cdots$	42.75	$\cdots$	NGC 3822	$\cdots$	$\cdots$	$\cdots$	$\cdots$
M-2-33-34	42.30	42.15	43.55	$\cdots$	NGC 3976	$\cdots$	39.77	43.22	$\cdots$
MKN 231	45.74	44.35	$\cdots$	42.51	NGC 3982	40.47	38.59	43.23	40.27
NGC 5033	39.86	40.92	$\cdots$	39.83	NGC 4303	$\cdots$	39.47	42.26	$\cdots$

Table 9—Continued

Seyfert 1	IR 10 μm	IR 2 μm	NUV 2267Å	HX 2-10 keV	Seyfert 2	IR 10 μm	IR 2 μm	NUV 2267Å	HX 2-10 keV
M-6-30-15	⋯	42.30	43.33	42.75	NGC 4388	42.18	41.82	42.38	42.62
IRAS 13349+2438	⋯	44.64	44.34	43.72	NGC 4501	⋯	40.86	⋯	40.03
UGC 08621	⋯	43.42	43.59	⋯	TOLOLO 1238-364	⋯	41.91	⋯	40.09
NGC 5252	⋯	⋯	43.21	⋯	NGC 4628	⋯	⋯	42.72	⋯
NGC 5273	⋯	⋯	⋯	41.36	NGC 4826	⋯	40.02	⋯	⋯
I4329A	⋯	⋯	43.36	43.81	NGC 4922	43.85	40.31	44.26	40.63
MKN 279	43.94	⋯	⋯	⋯	NGC 4941	39.91	38.97	41.31	41.47
NGC 5548	43.56	43.03	42.54	43.29	NGC 4869	⋯	41.56	43.71	⋯
MKN 471	⋯	⋯	⋯	⋯	NGC 5005	⋯	41.26	42.80	39.82
NGC 5674	⋯	⋯	42.95	⋯	M-3-34-64	⋯	⋯	⋯	⋯
MKN 817	⋯	43.38	43.50	⋯	NGC 5135	42.76	42.21	43.26	42.58
MKN 841	⋯	⋯	43.88	⋯	NGC 5194	38.67	38.38	41.29	40.99
IRAS F15091-2107	⋯	43.67	⋯	43.57	NGC 5248	⋯	38.96	⋯	⋯
NGC 5905	⋯	41.24	⋯	⋯	NGC 5256	43.78	42.60	43.97	43.28
CGCG 022-021	⋯	⋯	⋯	⋯	MKN 270	⋯	⋯	44.76	⋯
IRAS F16156+0146	⋯	⋯	⋯	⋯	NGC 5278	⋯	⋯	43.58	⋯
E141-G55	⋯	43.59	45.36	⋯	MKN 273	⋯	43.14	⋯	42.46
NGC 6860	⋯	42.62	⋯	⋯	MKN 796	⋯	42.37	⋯	⋯
MKN 509	44.60	43.73	⋯	43.86	MKN 1361	⋯	42.48	⋯	⋯
NGC 7213	⋯	41.78	⋯	42.03	MKN 461	⋯	⋯	⋯	⋯
E344-G16	⋯	43.54	44.07	⋯	NGC 5347	⋯	41.51	⋯	41.49
3c445	45.15	⋯	⋯	43.98	MKN 463	⋯	⋯	⋯	43.10
NGC 7314	⋯	41.27	⋯	41.33	NGC 5395	⋯	⋯	42.67	⋯
UGC12138	⋯	⋯	⋯	⋯	NGC 5506	42.23	⋯	42.17	44.04
NGC 7469	43.48	43.00	43.08	43.15	MKN 686	⋯	⋯	42.28	⋯
NGC 7603	44.03	43.56	43.19	41.59	NGC 5899	⋯	39.52	42.49	⋯

Note. —

Luminosities of Seyfert 1 and Seyfert 2 galaxies discussed in Appendix A, units are $Log(Luminosity)$ in erg/s. The Infrared data are obtained from the 2MASS catalogue, the Ultraviolet data are from GALEX, and the X-ray data are from Brightman & Nandra (2011a,b), and Panessa et al. (2008).

Table 10.   IR, NUV, and HX continuum vs. Optical Emission-Lines

Log L(Emission-Line)	Type	*IR* 10 μm	*IR* 2 μm	*NUV* 2267Å	*HX* 2-10 keV
Log L([O III] λ5007)	Sy 1	2.16 ± 1.23	1.55 ± 0.92	2.31 ± 0.61	1.64 ± 0.63
	Sy 2	2.07 ± 1.31	1.32 ± 1.61	2.76 ± 1.05	1.50 ± 1.01
Log L([O III] λ5007 + $H\beta$)	Sy 1	1.84 ± 1.17	1.22 ± 0.84	2.00 ± 0.62	1.34 ± 0.62
	Sy 2	2.00 ± 1.30	1.18 ± 1.33	2.64 ± 0.99	1.42 ± 1.02
Log L($H\alpha$)	Sy 1	1.22 ± 1.11	0.81 ± 0.85	1.76 ± 0.73	1.17 ± 0.52
	Sy 2	2.07 ± 1.18	1.14 ± 1.08	2.71 ± 0.85	1.34 ± 1.31
Log L($H\alpha$ +[N II])	Sy 1	1.09 ± 1.08	0.69 ± 0.88	1.62 ± 0.61	1.06 ± 0.55
	Sy 2	1.74 ± 1.26	0.85 ± 1.09	2.42 ± 0.85	1.05 ± 1.33

Note. — Results from least squares fit for $Log(L_{\mathrm{continuum}}) = Log(L_{\mathrm{emission-line}}) + B$ (discussed in Appendix A), where B is the intercept and the slope = 1. The Infrared data are obtained from the 2MASS catalogue, the Ultraviolet data are from GALEX, and the X-ray data are from Brightman & Nandra (2011a,b), and Panessa et al. (2008).